People's Democratic Republic of Algeria

Ministry of Higher Education and Scientific Research

University of Echahid Cheikh Larbi Tebessi-Tebessa

Material Sciences Department





MASTER'S THESIS

in

Condensed Matter Physics

By

Bouguerra Rahma **Traia Zahra**

Influence of Rare-earth metal doping on the electronic and magnetic properties of semiconductor

---

Date:June 11, 2025

Jury Members

Chairperson	Serdouk Fadila	MCA	Echahid Cheikh Larbi Tebessi, Tebessa University
Supervisor	Chemam Faïçal	Prof.	Echahid Cheikh Larbi Tebessi, Tebessa University
Examiner	Djabri Amina	MCB	Echahid Cheikh Larbi Tebessi, Tebessa University

2024/2025

People's Democratic Republic of Algeria

Ministry of Higher Education and Scientific Research

University of Echahid Cheikh Larbi Tebessi-Tebessa

Material Sciences Department



MASTER'S THESIS

in

Condensed Matter Physics

By

Bouguerra Rahma **Traia Zahra**

Influence of Rare-earth metal doping on the electronic and magnetic properties of semiconductor

---

Date:June 11, 2025

Jury Members

Chairperson	Serdouk Fadila	MCA	Echahid Cheikh Larbi Tebessi, Tebessa University
Supervisor	Chemam Faïçal	Prof.	Echahid Cheikh Larbi Tebessi, Tebessa University
Examiner	Djabri Amina	MCB	Echahid Cheikh Larbi Tebessi, Tebessa University

2024/2025

الإهداء

أهدي هذا العمل المتواضع إلى:

إلى والدي العزيز:

السند القوي ومعلمي الأول، ومصدر حكمتي وإلهامي. هذا العمل هو ثمرة جهدك وصبرك وتضحياتك التي قدمتها لي منذ نعومة مسامير. أسأل الله أن يطيل عمرك ويجعلك من السعداء في الدارين.

إلى ...

إلى والدتي الحبيبة:

مصدر الحنان والعطاء، التي كانت دائماً سندي وداعمي في كل خطوة. دعواتك وتشجيعك كانا النور الذي أضاء لي الطريق. أسأل الله أن يبارك في عمرك ويمنحك الصحة والسعادة.

محمد ...

إلى إخوتي وأخواتي:

رفيق درب ومصدر قوتي في الأوقات الصعبة. دعمكم وإيمانكم بقدراتي كان دائماً سبباً في استمراري. أهدي لكم هذا العمل راجياً أن يكون مصدر فخر لكم ولأولادكم من بعدكم.

فهيمة .. أمل .. دعاء .. الناس .. محمد ...

إلى شريكتي في العمل، رحمة:

رفيقة الدرب وشريكة النجاح، التي لم تبخل علي بدعمها وتشجيعها. شكراً لكل لحظة تعاون وجهد مشترك، وإلى ذلك كل الوفاء والحب.

إلى أصدقاء الدراسة:

لكل من كان لهم هذه الرحلة وسلاسلها، أهديكم هذا الجهد مع الشكر والتقدير.

إلى كل من علمني وجهني نصحني:

أشكركم لكم جميعا، ولكم السلام وصولا إلى هذه اللحظة.

شهرة...

أهدي هذا العمل المتواضع إلى

إلى والدي العزيز

شكرا من القلب على حبكما اللا متناهي ونصائحكما التي لا تقدر. كنتما دائما سندي القوي وملاذي الآمن. لقد ساهمتما في

دعواتكما ودعمكما القوي طوال هذه الرحلة. أسأل الله أن يرزقكما الصحة وطول العمر والسعادة.

إلى أخواتي وأخواتي الأعزاء

أنتم رفقاء درب مدى الحياة، ومصدر راحتي وسعادتي. كان دعمكم المستمر وتشجيعكم دافعا لي للاستمرار. شكرا لوقوفكم الدائم

إلى جانبي. أتمنى لكم دائما القوة والسعادة.

إلى أصدقائي وصديقاتي العزيزة، زهرة

أشكركم جميعا وصديقتي وسام، أتمنى أن تكون هذه الرحلة كل صديق كما تتمناه وتعاونك البشر الكثير. هذا النجاح مهما

كان صغيرا لوجودك ودعمك إلى لك دوام التوفيق والسعادة.

إلى أصدقاء الأعزاء

إلى كل من ساعدني ووقف إلى جانبي، أهديكم هذا النجاح كل امتنان، مع تطلعي الدائم أن أستمر في مشاركتكم

إلى كل من علمني حرفا أو قدم النصيحة

شكرا لكم جميعا على مساعدتكم وتشجيعكم. تم السير بنجاح وصولا إلى هذه المرحلة

رحمة...

Acknowledgments

We think about it a lot during the writing process, but there is much work to be done before reaching this point. Finally, the time has come to express our deep gratitude to everyone who contributed to this work. We express our deepest gratitude to Almighty Allah, who granted us the strength to complete this humble work and illuminated our path in the pursuit of knowledge. We also extend our heartfelt thanks and appreciation to our supervisor, **Professor Faïçal Chemam**, for his excellent guidance, valuable advice, and constant support throughout the course of this research. Our sincere gratitude goes to the members of the defense committee, the **Chairwoman: Dr. Sardouk Fadhila** and the examiner **Dr. Djabri Amina**. We also extend our gratitude to all the professors of the Department of Material Sciences who contributed to our academic formation. Finally, we thank everyone who played a role in the completion of this work, even if their names were not mentioned here. May Allah reward them all. **Zahra ... Rahma**

ABSTRACT

This theoretical study investigates the influence of rare-earth (Gd, Tb, Eu) doping on the electronic and magnetic properties of zinc oxide (ZnO) using first-principles calculations based on Density Functional Theory (DFT) implemented in the WIEN2k code. The modified Becke-Johnson (TB-mBJ) potential was employed to accurately predict electronic properties. Structural optimization revealed dopant-dependent lattice modifications, with Tb causing the most significant distortion. Electronic structure analysis showed band gap variations and Fermi level shifts characteristic of n-type semiconductors. Magnetic properties calculations demonstrated that Gd and Tb doping induces substantial magnetic moments through their unpaired 4f electrons, with Tb-doped ZnO exhibiting partially half-metallic behavior. These findings provide fundamental insights for designing ZnO-based materials for spintronic and optoelectronic applications.

Keywords: ZnO, rare-earth doping, DFT, electronic structure, magnetic properties, WIEN2k

RESUME

Cette étude théorique examine l'influence du dopage par des terres rares (Gd, Tb, Eu) sur les propriétés électroniques et magnétiques de l'oxyde de zinc (ZnO) à l'aide de calculs de premiers principes basés sur la théorie de la fonctionnelle de la densité (DFT) implémentée dans le code WIEN2k. Le potentiel modifié de Becke-Johnson (TB-mBJ) a été employé pour prédire avec précision les propriétés électroniques. L'optimisation structurale a révélé des modifications du réseau dépendantes du dopant, le Tb causant la distorsion la plus importante. L'analyse de la structure électronique a montré des variations de bande interdite et des déplacements du niveau de Fermi caractéristiques des semi-conducteurs de type n. Les calculs des propriétés magnétiques ont démontré que le dopage par Gd et Tb induit des moments magnétiques importants grâce à leurs électrons 4f non appariés, avec un comportement semi-métallique partiel pour le ZnO dopé au Tb. Ces résultats fournissent des informations fondamentales pour la conception de matériaux à base de ZnO destinés à des applications en spintronique et optoélectronique.

Mots-clés: ZnO, dopage par terres rares, DFT, structure électronique, propriétés magnétiques, WIEN2k

ملخص

تبحث هذه الدراسة النظرية في تأثير التطعيم بالمعادن الترابية (Gd, Eu, Tb) على الخواص الإلكترونية والمغناطيسية لأكسيد الزنك (ZnO) باستخدام حسابات المبادئ الأولى القائمة على نظرية الكثافة الوظيفية (DFT) المطبقة في كود WIEN2k. تم استخدام كمون Becke-Johnsonالمعدلة (TB-mBJ) للتنبؤ بدقة بالخصائص الإلكترونية. كشف تحسين البنية البلورية عن تعديلات شبكية تعتمد على العناصر الترابية المطعمة، حيث تسبب Tb في أهم تشويه. أظهر تحليل البنية الإلكترونية تغيرات في فجوة النطاق وتحولات مستوى فيرمي المميزة لأشباه الموصلات من النوعn . أظهرت حسابات الخواص المغناطيسية أن التطعيم بـ Tb يستحدث مغناطيسية كبيرة من خلال إلكترونات 4f حيث يُظهر ZnO المطعم بـ Tb سلوكًا نصف معدني جزئياً. وتوفر هذه النتائج رؤى أساسية لتصميم المواد القائمة على ZnO أو للتطبيقات الإلكترونية البصرية.

List of Figures

1.1 Energy band diagram of a conductor, an insulator, and a semiconductor. 7

1.2 Conduction mechanism in intrinsic semiconductors: (a) Without an electric field, (b) Under the influence of an electric field. 8

1.3 Variation of free carrier concentration with temperature. 9

1.4 Concept of electrons and holes in semiconductors. 10

1.5 Valence and conduction bands for: (a) a pure (intrinsic) semiconductor; (b) a semiconductor with ntype doping; and (c) a semiconductor with p-type doping. The • and ◦ symbols represent free electrons and holes respectively. The Fermi energies of the n- and p-type samples lie very close in energy to the impurity levels arising from the donor or acceptor atoms respectively[8]. 11

1.6 Extrinsic semiconductor. 14

1.7 Figure : Structures of ZnO 18

1.8 Band Structure of ZnO Wurtzite[16] 20

2.1 The auto-coherent Kohn-Sham diagram. 30

2.2 Muffin-Tin potential 35

2.3 exemple of multiple energy windows. 39

2.4 Wien2k structure. 42

3.1 **ZnO structure with and without Rare-earth doped and top view image** 45

3.2 **Optimization Curve of ZnO** 47

3.3 **Optimization Curve of** $Zn_{15}EuO_{16}$ 49

3.4 **Optimization Curve of** $Zn_{15}GdO_{16}$ 49

3.5 **Optimization Curve of** $Zn_{15}TbO_{16}$ 50

3.6 **Total density of state and band structures of** $Zn_{16}O_{16}$ 52

3.7 **PDOS of $Zn_{16}O_{16}$ with mBJ (b) and without mBJ (a)** 54
3.8 **Total density of state and band structures of $Zn_{15}GdO_{16}$** 55
3.9 **PDOS of $Zn_{15}GdO_{16}$ without mBJ (a) and with mBJ (b)** 57
3.10 **Total density of state and band structures of $Zn_{15}TbO_{16}$** 58
3.11 **PDOS of $Zn_{15}TbO_{16}$ with mBJ (a) and without mBJ (b)** 60
3.12 **Total density of state and band structures of $Zn_{15}EuO_{16}$** 61
3.13 **PDOS of $Zn_{15}EuO_{16}$ with mBJ (a) and without mBJ (b)** 63

List of Tables

1.1 Physical Parameters of ZnO 19

3.1 **Theoretical and experimental structural parameters of rare earth-doped ZnO.** 51

3.2 Comparison of band gaps (in eV) for pure and RE-doped ZnO 62

3.3 Comparison of spin magnetic moments (in μ_B) for RE-doped ZnO compounds from this work and Hachimi et al. (2014)[107] 64

0.1 List of Abbreviations and Symbols

DFT	Density Functional Theory
GGA	Generalized Gradient Approximation
LDA	Local Density Approximation
PBE	Perdew-Burke-Ernzerhof (DFT functional)
TB-mBJ	Tran-Blaha modified Becke-Johnson (potential)
FP-LAPW	Full-Potential Linearized Augmented Plane Wave (method)
WIEN2k	Software package for DFT calculations
ZnO	Zinc Oxide
RE	Rare Earth
DOS	Density of States
PDOS	Projected Density of States
TDOS	Total Density of States
VBM	Valence Band Maximum
CBM	Conduction Band Minimum
SOC	Spin-Orbit Coupling
DMS	Diluted Magnetic Semiconductor
TCO	Transparent Conductive Oxide
LED	Light-Emitting Diode
UV	Ultraviolet
SCF	Self-Consistent Field (cycle)
BZ	Brillouin Zone
MT	Muffin-Tin (sphere)
E_F	Fermi Energy
ε_g	Bandgap energy (eV)
$\rho(\mathbf{r})$	Electron charge density

Rare Earth Elements

Gd	Gadolinium
Tb	Terbium
Eu	Europium

Technical Terms

APW	Augmented Plane Wave (method)
LMTO	Linear Muffin-Tin Orbital (method)
PP-PW	Pseudopotential Plane-Wave (method)
KKR	Korringa-Kohn-Rostoker (method)
LSTART	Initialization step in WIEN2k for atomic densities
KGEN	K-point mesh generation in WIEN2k
DSTART	Initial charge density generation in WIEN2k
LAPW0/1/2	Modules in WIEN2k for potential, eigenvalues, and charge density
LCORE	Core state calculation in WIEN2k
MIXER	Charge density mixing in WIEN2k

Units

eV	Electronvolt
Ry	Rydberg (unit of energy)
Å	Angstrom (unit of length)
μ_B	Bohr magneton (unit of magnetic moment)

Symbols in Equations

n	Electron concentration
p	Hole concentration
n_i	Intrinsic carrier concentration
E_c/E_v	Conduction/Valence band energy
E_{Fi}	Fermi level in intrinsic semiconductor
U_{eff}	Effective Hubbard parameter (DFT+U)

Contents

Acknowledgments v

ABSTRACT vii

RESUME vii

List of Figures x

List of Tables xi

0.1 List of Abbreviations and Symbols . . .

General Introduction 1

GENERAL INTRODUCTION 1

1 State of the Art 4

1.1 Semiconductors . . . 5

1.2 Introduction . . . 5

1.3 Classification of Materials . . . 5

1.3.1 Insulators . . . 6

1.3.2 Semiconductors . . . 6

1.3.3 Conductors . . . 7

1.4 Intrinsic Semiconductors . . . 8

1.4.1 Definition . . . 8

1.4.2 Generation of Electron-Hole Pairs . . . 10

1.5 Extrinsic Semiconductors . . . 10

1.6 Classification of Extrinsic Semiconductors . . . 12

1.6.1 N-Type Semiconductor . . . 12

1.6.2 P-Type Semiconductor 13
1.7 Diluted Magnetic Semiconductors (DMS) 13
1.7.1 Semiconductor Lattices with Magnetic Elements 13
1.7.2 Performance Characteristics of Magnetic Semiconductors 15
1.8 Fundamental Characteristics of Zinc Oxide (ZnO) 15
1.8.1 Physical and Chemical Properties 16
1.8.2 Structural and Electronic Properties 16
1.8.3 Electronic Properties: 17
1.9 Doping of ZnO Material 18

2 METHODOLOGY **21**
2.1 The equation of Schrödinger and problem of several particles 22
2.1.1 Born-Oppenheimer approximation (1927) 23
2.1.2 Hartree and Hartree-Fock approximation (1928-1930) 25
Density functional theory (DFT) 26
2.2 Hohenberg-Kohn theorems 27
2.3 Kohn-Sham equations 28
2.4 Resolution of Equations 29
2.5 The exchange correlation functional 31
2.6 The local density approximation (LDA) 31
2.7 Generalized Gradients Approximation(GGA) 32
2.8 DFT+U approximation 33
2.9 Spin-Orbit Coupling (SOC) 34
Augmented and Linearized Plane Wave Method (FP-LAPW) 34
2.10 The method (APW) 34
2.11 FP-LAPW method 37
2.12 Modification of FP-LAPW 38
2.12.1 Multiple energy windows 38
2.12.2 Local orbitals 39
2.12.3 The concept of FP-LAPW 39
2.13 WIEN2k code 40

2.13.1 Initialization (Computational Detail) 40
2.13.2 Self-consistent cycle (SCF) 41

3 Results and Discussion **43**
3.1 Introduction 44
3.2 Computational Methodology 44
3.3 Results 45
3.3.1 Structural parameters 45
3.3.2 Optimization 46
3.3.3 Electronic Structure 51
3.3.4 Magnetic properties 63
3.3.5 Structural Modifications: 65
3.3.6 Electronic Properties: 65
3.3.7 Magnetic Properties: 65
3.3.8 Comparative Analysis: 65

General Introduction

Zinc oxide (ZnO), a II–VI compound semiconductor, has garnered significant attention due to its exceptional blend of physical, chemical, and optoelectronic characteristics. Featuring a direct wide band gap of approximately 3.3 eV at room temperature, a high exciton binding energy (60 meV), strong optical absorption, excellent transparency in the visible spectrum, and impressive thermal and chemical stability, ZnO is considered a highly versatile material for various industrial and research applications. These range from transparent conductive oxides (TCOs), UV light-emitting diodes (LEDs), and laser diodes, to gas sensors, piezoelectric devices, and thin-film transistors. Moreover, the material's compatibility with environmentally benign substances and low-cost processing techniques has further reinforced its potential in photovoltaic and advanced optoelectronic systems. Nevertheless, despite its favorable optical properties, intrinsic ZnO suffers from limited electrical conductivity and lacks inherent magnetic behavior—constraints that hinder its applicability in spintronic and multifunctional devices.

To overcome these limitations and expand ZnO's functional landscape, several strategies have been explored, with doping emerging as one of the most promising approaches. Traditional doping with group III elements such as Al, Ga, and In has successfully enhanced n-type conductivity, but these elements do not induce magnetic characteristics. Alternatively, doping with rare earth (RE) elements has opened new pathways—not only for tuning the electronic properties but also for introducing and controlling magnetic interactions within the ZnO matrix. Owing to their partially filled and well-shielded 4f orbitals, RE ions possess unique magnetic and luminescent properties, which are relatively insensitive to the surrounding crystal field. The shielding by outer 5s and 5p electrons stabilizes the 4f electronic configuration, resulting in sharp emission lines and prolonged

excited-state lifetimes. When incorporated into the ZnO lattice, RE elements can interact with host electrons to induce spin polarization, magnetic ordering, and modifications in the electronic band structure—features essential for spintronic and multifunctional applications.

Specifically, RE elements such as Gadolinium (Gd), Terbium (Tb), and Europium (Eu) have shown distinct effects on the structural, electronic, and magnetic behavior of ZnO. Gd is well-known for its high magnetic moment and its role in promoting long-range ferromagnetic interactions. Tb provides a compelling balance between magnetic and optical functionalities, while Eu stands out for its strong red luminescence and notable electron correlation effects. These dopants can integrate into the ZnO crystal structure while introducing localized states that interact with the conduction and valence bands. Experimental observations have revealed enhancements in photoluminescence, electrical conductivity, and the emergence of new magnetic phases upon RE doping. However, the underlying mechanisms driving these improvements—especially those related to defect formation, electronic structure evolution, and magnetic exchange—remain not fully understood.

In this thesis, we present a comprehensive theoretical study on ZnO doped with Gd, Tb, and Eu, utilizing first-principles calculations based on Density Functional Theory (DFT). Our simulations are carried out using the WIEN2k code, which employs the Full Potential Linearized Augmented Plane Wave (FP-LAPW) method—recognized for its accuracy in studying solid-state systems. To overcome the typical underestimation of the band gap in standard DFT, we apply the modified Becke-Johnson (TB-mBJ) exchange potential, known for producing more accurate band structure predictions. This study aims to explore the influence of RE doping on structural stability, electronic and magnetic properties of ZnO. By evaluating these aspects across different doping elements, we seek to offer valuable insights into the design of multifunctional ZnO-based materials for advanced spintronic and optoelectronic devices.

The first chapter introduces the theoretical background, covering the intrinsic properties of ZnO, the fundamentals of diluted magnetic semiconductors (DMS), and the role of rare earth doping. This framework sets the stage for the subsequent chapters, which

detail the computational methodology, analyze and discuss the simulation results, and compare them with existing experimental and theoretical findings. Ultimately, this work contributes to the broader understanding of RE-doped semiconductors and supports ongoing efforts in the development of customized materials for emerging nanotechnologies.

Chapter 1

State of the Art

- **An Overview of semiconductor.**
- **Diluted Magnetic Semiconductors (DMS).**
- **Fundamental Characteristics of Zinc Oxide (ZnO).**

1.1 Semiconductors

1.2 Introduction

The exploration of semiconductor materials began in the early 19th century, heralding the dawn of a technological revolution. Over the past two centuries, numerous semiconductors have been studied, with silicon (Si) and germanium (Ge) emerging as key materials. These elemental semiconductors consist of uniform atomic compositions, in contrast to compound semiconductors like gallium arsenide (GaAs) which combine Group III (gallium) and Group V (arsenic) elements. This strategic combination of elements enables unique electrical and optical characteristics unattainable in pure elemental semiconductors [1, 2].

Germanium, discovered by Clemens Winkler on February 6, 1886, played a pioneering role in early semiconductor applications. Despite its historical importance, germanium's utility is constrained in modern applications demanding either minimal power consumption or high-temperature stability. This limitation led to its gradual replacement in the 1970s[3, 4].

In contrast, silicon - first isolated by J.J. Berzelius in Stockholm (1824) - has maintained unparalleled dominance in semiconductor technology since the 1960s. Its widespread adoption stems from an optimal combination of economical production costs and superior performance in low-power electronic applications [5].

1.3 Classification of Materials

Solid-state materials can be fundamentally categorized based on their electronic band structure and conduction properties into three distinct classes: insulators, semiconductors, and metals [2]. This classification stems from their characteristic energy band configurations and corresponding electrical behaviors.

1.3.1 Insulators

Insulators represent materials with a completely filled valence band and an empty conduction band, separated by a substantial energy gap (typically >5 eV). This band gap significantly exceeds thermal energy scales at room temperature ($kT \approx 0.026$ eV), creating an effective barrier to electron excitation. Consequently, insulators lack accessible energy states for charge carriers, rendering them incapable of supporting electrical conduction under normal conditions. This fundamental behavior is depicted schematically in Figure (1-1a).

1.3.2 Semiconductors

Semiconductors occupy a unique position between insulators and metals, exhibiting temperature-dependent conductivity that distinguishes them from both. At absolute zero ($T = 0$ K), their electronic structure resembles that of insulators - with a completely filled valence band and an empty conduction band. However, their distinguishing feature is the relatively narrow band gap (e.g., 1.12 eV for silicon, compared to several eV in insulators), as illustrated in Figure **(1-1b)** [6].

The electrical properties of semiconductors demonstrate remarkable temperature sensitivity. As thermal energy increases:

- Electrons gain sufficient energy to bridge the band gap, transitioning from valence to conduction band
- These promoted electrons become mobile charge carriers under applied electric fields
- The resulting vacancies (holes) in the valence band contribute additional conduction pathways

This dual carrier mechanism (electrons and holes) leads to the characteristic increase in conductivity with temperature - a behavior diametrically opposed to that observed in metals. The concentration of both carrier types grows exponentially with temperature, following well-defined statistical distributions that govern semiconductor device

operation.

1.3.3 Conductors

Conductors are materials characterized by the absence of a bandgap; their upper energy band is only partially filled. Typical examples include alkali metals such as lithium (Li), sodium (Na), potassium (K), rubidium (Rb), and cesium (Cs). In these materials, the valence band and conduction band overlap, enabling electrons to transition freely between them. Consequently, even at low temperatures, conduction electrons are present and mobile. When an external electric field is applied, these electrons can move with ease, resulting in the high electrical conductivity that defines conductive materials. This phenomenon is illustrated in Figure **(1-1c)**.

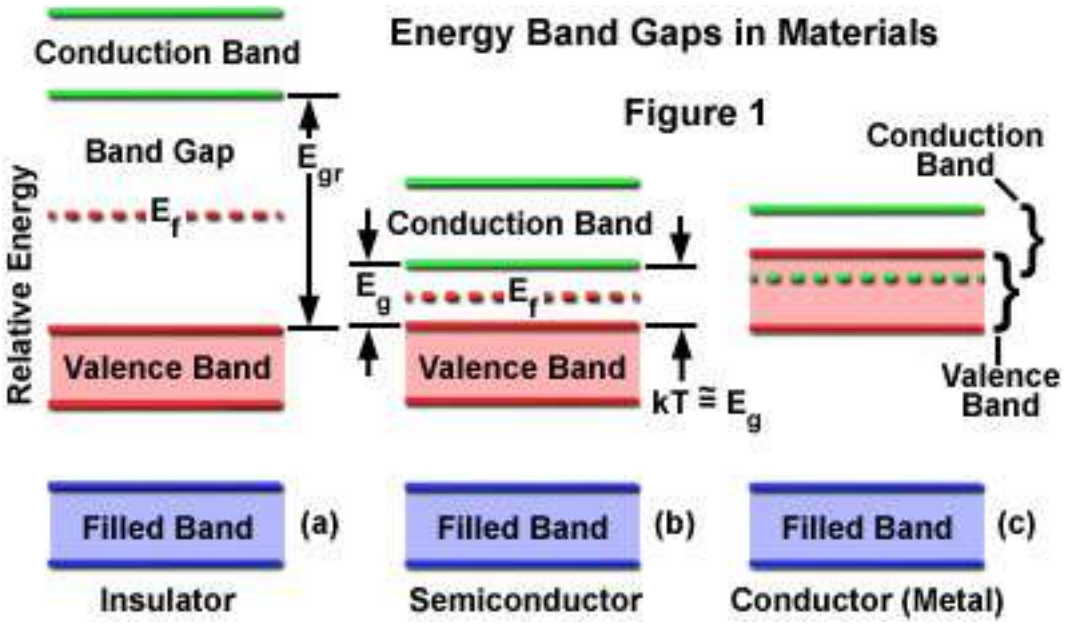


Figure 1.1: Energy band diagram of a conductor, an insulator, and a semiconductor. [2]

1.4 Intrinsic Semiconductors

1.4.1 Definition

An intrinsic semiconductor refers to a pure, defect-free material such as a perfect crystal of silicon or germanium, containing no impurities that might influence the density of charge carriers. These monocrystalline structures exhibit a tetrahedral geometry, with each atom symmetrically bonded to four neighboring atoms, as illustrated in Figure 1-2. In such materials, electrons in the conduction band arise solely through thermal excitation from the valence band. As a result, electrons and holes are generated in equal numbers, ensuring overall charge neutrality .

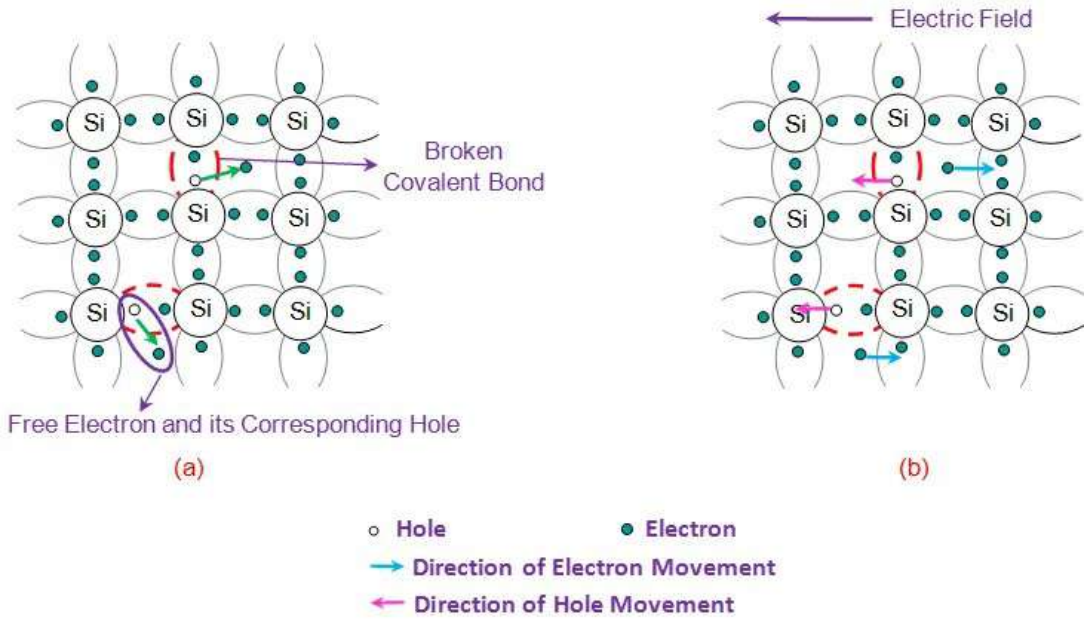


Figure 1.2: Conduction mechanism in intrinsic semiconductors: (a) Without an electric field, (b) Under the influence of an electric field.

In the context of semiconductor physics, the carrier concentrations in the conduction and valence bands are described by the following expressions:

$$n = n_c e^{-(E_c - E_f)/kT}$$

$$p = n_v e^{-(E_f - E_v)/kT}$$

Combining these equations yields the intrinsic carrier concentration:

$$n_i^2 = n \cdot p = n_c \cdot n_v \cdot e^{-E_g/kT} \quad (1.3)$$

where:

- n_i is the intrinsic carrier concentration,
- n and p are the electron and hole concentrations, respectively,
- n_c and n_v are the effective densities of states in the conduction and valence bands.

Thus, the intrinsic carrier density can also be written as:

$$n_i = \sqrt{n_c n_v} \cdot e^{(-E_g/2kT)} \quad (1.4)$$

An intrinsic semiconductor has a unique behavior dependent on temperature. It is often described as a poor conductor or an imperfect insulator; however, its electrical conductivity increases with temperature due to the rise in thermally generated charge carriers. The temperature dependence of carrier concentration is illustrated in Figure **(1-3)**.

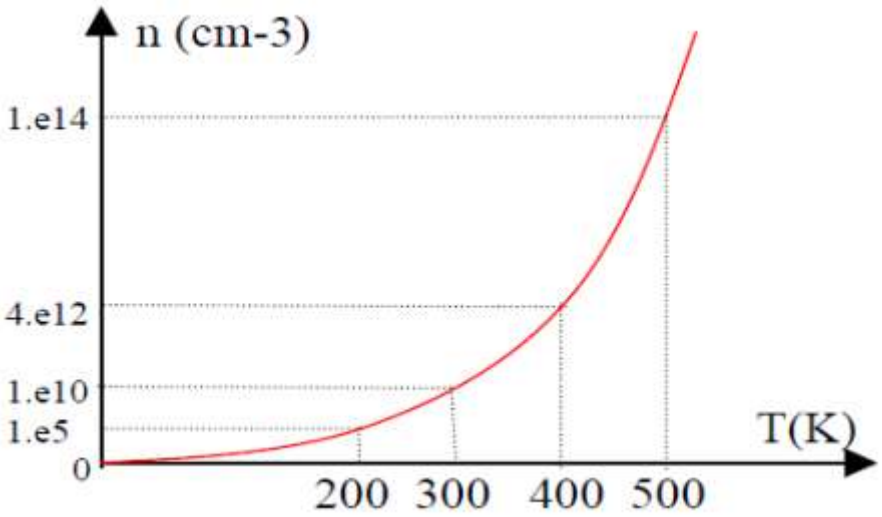


Figure 1.3: Variation of free carrier concentration with temperature.

Accordingly, the conductivity of an intrinsic semiconductor is closely linked to the number of thermally excited charge carriers. The position of the Fermi level in an intrinsic

material lies near the midpoint of the energy band gap and is given by:

$$E_{fi} = \frac{E_c - E_v}{2} + \frac{k_B T}{2} \log\left(\frac{n_c}{n_v}\right) \quad (1.5)$$

At room temperature, the Fermi level can be approximated as:

$$E_{fi} = \frac{E_c + E_v}{2} \quad (1.6)$$

1.4.2 Generation of Electron-Hole Pairs

At absolute zero (0 K), an intrinsic semiconductor acts as an insulator. As the temperature increases, valence electrons in the semiconductor absorb thermal energy. Some of these electrons gain enough energy to break free from the attraction of their parent atoms, becoming mobile within the crystal. This process, called the breaking of covalent bonds, generates free electrons.

In the presence of an external electric field, these free electrons contribute to electrical conductivity. Additionally, the breaking of bonds creates ionized atoms, which are electron-deficient and act as "holes." These holes behave as positive charges, equal in magnitude to the charge of an electron.

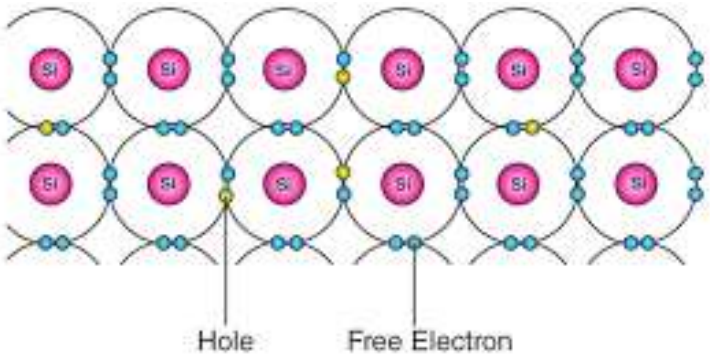


Figure 1.4: Concept of electrons and holes in semiconductors.

1.5 Extrinsic Semiconductors

The conductivity of semiconductors can be greatly enhanced by introducing a small number of replacement atoms known as impurities. This process is called doping. Typically,

only 1 atom in 10^7 is replaced by a dopant atom in a doped semiconductor. Extrinsic semiconductors are classified into two types [7]:

- N-type semiconductor,
- P-type semiconductor.

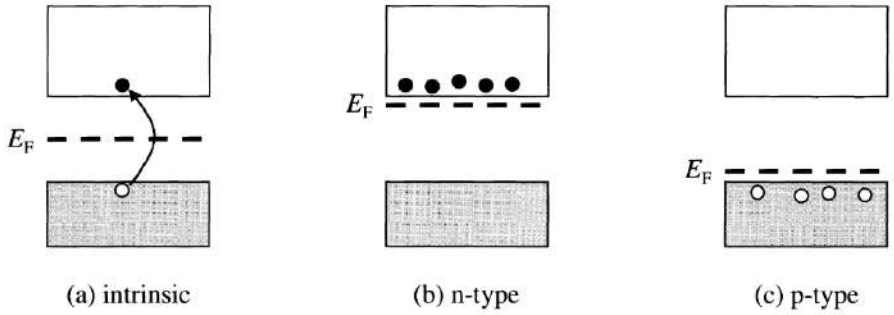


Figure 1.5: Valence and conduction bands for: (a) a pure (intrinsic) semiconductor; (b) a semiconductor with ntype doping; and (c) a semiconductor with p-type doping. The • and ◦ symbols represent free electrons and holes respectively. The Fermi energies of the n- and p-type samples lie very close in energy to the impurity levels arising from the donor or acceptor atoms respectively[8].

This Figure illustrates the behavior of the Fermi level in intrinsic and doped semiconductors [8]:

(a) Intrinsic semiconductor: In a pure crystal, the Fermi level lies midway between the conduction and valence bands. Thermal excitation promotes electrons to the conduction band, leaving behind holes in the valence band. Both electrons and holes contribute to electrical conduction, which is called intrinsic conductivity.

(b) n-type semiconductor: Doping the crystal with atoms (which have extra electrons) introduces donor levels just below the conduction band. The Fermi level shifts upward, near the donor levels. These electrons are easily excited into the conduction band, and the conductivity is dominated by these extrinsic electrons.

(c) p-type semiconductor: Doping with atoms from group III (which have fewer electrons) introduces acceptor levels just above the valence band. The Fermi level shifts downward,

near these acceptor levels. Electrons from the valence band fill these acceptor states, leaving holes in the valence band, which become the primary charge carriers.

1.6 Classification of Extrinsic Semiconductors

1.6.1 N-Type Semiconductor

- Dominated by electrons as charge carriers.
- The overall crystal remains neutral.
- Current components: $I = I_e$ and $n_h << n_e$.
- Majority carriers: Electrons.
- Minority carriers: Holes.

When a pure semiconductor (such as silicon or germanium) is doped with a pentavalent impurity (e.g., P, As, Sb, Bi), four of the five valence electrons of the impurity atom bond with the four electrons of the semiconductor. The fifth electron is free to move, making it available for conduction.

- These dopant atoms are known as donors because they donate free electrons to the lattice.
- The addition of impurities increases the number of negative charge carriers, hence the term n-type semiconductor.
- The crystal as a whole remains neutral, but the donor atom becomes an immobile positive ion.
- Since conduction is dominated by free electrons, electrons are the majority carriers, while holes are the minority carriers.

1.6.2 P-Type Semiconductor

- Dominated by holes as charge carriers.
- The overall crystal remains neutral.
- Current components: $I = I_h$ and $n_h \gg n_e$.
- Majority carriers: Holes.
- Minority carriers: Electrons.

When a pure semiconductor is doped with a trivalent impurity (e.g., B, Al, In, Ga), the three valence electrons of the impurity bond with three of the four valence electrons of the semiconductor. This leaves one valence electron of the semiconductor unbonded, creating a hole (absence of an electron).

- These dopant atoms are called acceptors because they accept electrons to fill the hole.
- The addition of impurities increases the number of positive charge carriers (holes), hence the term p-type semiconductor.
- The crystal as a whole remains neutral, but the acceptor atoms become immobile negative ions.
- Since conduction is dominated by holes, holes are the majority carriers, while electrons are the minority carriers.

1.7 Diluted Magnetic Semiconductors (DMS)

1.7.1 Semiconductor Lattices with Magnetic Elements

Diluted Magnetic Semiconductors (DMS) represent a unique class of materials that combine semiconductor properties with magnetic functionality. These hybrid materials enable

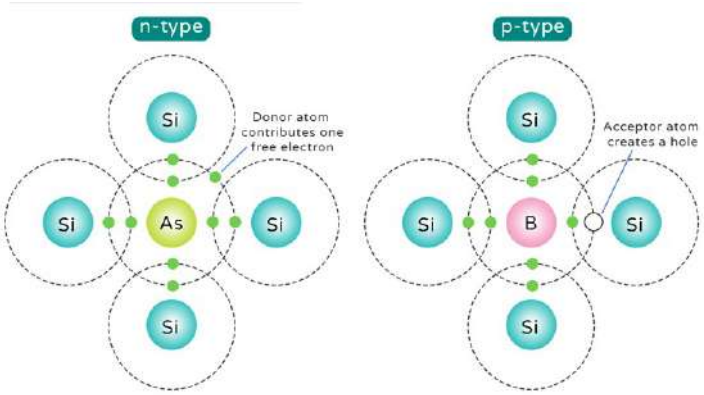


Figure 1.6: Extrinsic semiconductor.

precise control of spin-related phenomena while preserving their semiconducting characteristics.

The term "diluted" reflects the low concentration of magnetic elements (typically transition metals) incorporated into the semiconductor matrix. This strategic doping modifies spin interactions without significantly disrupting the host material's electronic structure [9].

In DMS systems, magnetic atoms with localized moments replace a fraction of atoms in conventional semiconductor lattices, introducing magnetic ordering such as spin glass phases. The study of these materials originated in the 1960s with the observation of magnetic phenomena in semiconductors containing magnetic impurities.

Significant progress occurred in the 1970s through doping of II-VI semiconductors (e.g., CdTe, ZnSe). These systems exhibit paramagnetic behavior at low doping concentrations and transition to antiferromagnetic ordering at higher concentrations.

A breakthrough came in 1997 with the demonstration of carrier-induced ferromagnetism in p-type CdMnTe quantum wells, proving that magnetic properties could be controlled through charge carrier modulation [10]. Further developments involved III-V semiconductors like Mn-doped InAs, where Mn acts as an acceptor dopant to establish stable ferromagnetic interactions [11].

1.7.2 Performance Characteristics of Magnetic Semiconductors

Certain semiconductors play a crucial role in spintronic applications for data storage, sensing, and optoelectronic devices. While conventional semiconductors (Si, Ge, GaAs, GaN) dominate microelectronics, their magnetic counterparts require doping with magnetic ions (e.g., Mn) to introduce spin-dependent functionality.

In DMS materials, magnetic dopants facilitate ferromagnetic coupling between localized moments and delocalized carriers. Current technological limitations include [12]:

- Low charge carrier densities
- Limited magnetic moment densities
- Curie temperatures below room temperature

ZnO-Based DMS Materials

While zinc oxide (ZnO) has traditional applications in chemical and pharmaceutical industries, its remarkable properties have sparked interest for advanced technologies:

- Exceptional thermal properties (high conductivity and heat capacity)
- Moderate dielectric constant
- High resistivity with low water absorption
- Strong UV absorption capabilities

These characteristics make ZnO particularly promising for developing multifunctional devices [13].

1.8 Fundamental Characteristics of Zinc Oxide (ZnO)

Zinc oxide (ZnO) is an inorganic compound that occurs naturally as the mineral zincite. First identified in 1810 in New Jersey, USA, it has become the most commercially sig-

nificant zinc compound. For most applications, ZnO requires synthetic production to achieve desired specifications [14].

The material's versatility enables diverse applications in:

- Optoelectronic and acousto-optic devices
- Piezoelectric systems
- Catalytic applications
- Gas sensing technologies

1.8.1 Physical and Chemical Properties

ZnO exhibits several distinctive characteristics that make it valuable for technological applications:

Electronic Properties

- **Band Structure**: Direct bandgap semiconductor with 3.37 eV gap at room temperature
- **Exciton Effects**: High binding energy (60 meV) enhances optoelectronic performance

Chemical Behavior

- **Biocompatibility**: Non-toxic nature enables biomedical applications
- **Environmental Stability**: Excellent thermal and chemical resistance

1.8.2 Structural and Electronic Properties

Zinc oxide (ZnO) is considered a challenging material for beginners in materials science due to its multifunctional nature and a wide range of unique properties. It has been ex-

tensively studied, making it an excellent starting point for understanding other materials, thanks to its outstanding characteristics and diverse applications.

ZnO can crystallize in three different structures: wurtzite, zinc blende, and rock salt. However, under standard temperature and pressure conditions, the thermodynamically stable structure is the wurtzite form, with ionicity lying between covalent and ionic semiconductors. This hexagonal structure belongs to the $P6_3mc$ space group in Hermann–Mauguin notation or the C_{6v} class in Schoenflies notation. The primitive unit cell of ZnO contains two formula units, where each zinc atom is tetrahedrally coordinated by four oxygen atoms and vice versa, as shown in Figure **(1-7)**.

This non-centrosymmetric tetrahedral arrangement is responsible for the material's piezoelectric behavior, crystal polarity, and also plays a crucial role in crystal growth and defect formation.

The wurtzite ZnO structure presents four commonly observed crystal faces: the polar (0001) faces terminated with either Zn or O atoms (along the c-axis), and the non-polar $(10\bar{1}0)$ and $(11\bar{2}0)$ faces (along the a-axis), which contain an equal number of Zn and O atoms. Among these, the polar and $(10\bar{1}0)$ surfaces are relatively stable, while the $(11\bar{2}0)$ face is considered less stable.

Lattice parameters of ZnO are typically measured at room temperature using X-ray diffraction (XRD). The values are approximately a = 3.25 Å and c = 5.20 Å, yielding an ideal c/a ratio of 1.6. However, slight variations may occur depending on the presence of impurities, defects, external stress, or temperature fluctuations.

1.8.3 Electronic Properties:

the relatively wide band gap of ZnO (approximately 3.37 eV) limits its light absorption efficiency under solar irradiation to around 4 percent , which reduces its photocatalytic effectiveness in the visible spectrum.

The electronic band structure and density of states of wurtzite-structured ZnO have been studied both theoretically and experimentally. In the valence band, the energy levels between –10 eV and –5 eV mainly correspond to Zn 3d orbitals, while the upper

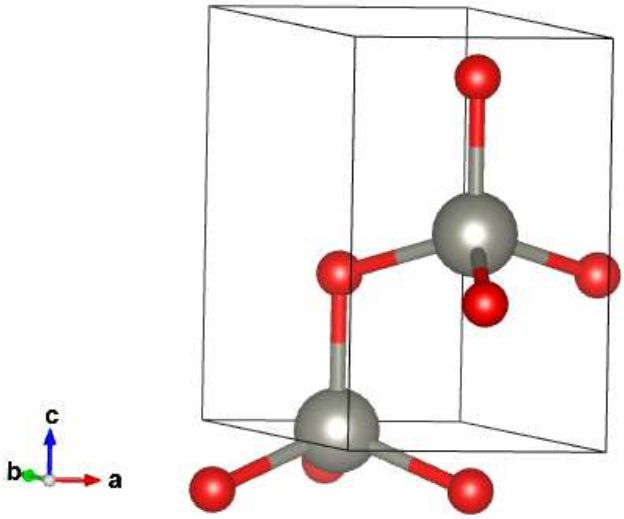


Figure 1.7: Figure : Structures of ZnO

valence bands from –5 eV to 0 eV are dominated by O 2p orbitals. In the conduction band, the lowest two bands originate primarily from the unoccupied Zn 4s orbitals. The calculated band gap using this method was reported to be 3.77 eV .

The electronic configurations of Oxygen and Zinc are:

$$1s^2 2s^2 2p^4$$

$$1s^2 2s^2 2p^6 3s^2 3p^6 3d^{10} 4s^2$$

1.9 Doping of ZnO Material

A semiconductor is a crystalline solid whose electrical conductivity properties are primarily defined by two distinct energy bands:

The valence band ; containing electrons involved in covalent bonds between atoms.

The conduction band ; holding electrons in an excited state that can move freely through the crystal lattice There are two type of semiconductor:

Physical Parameter	**Value**
Crystal structure	Wurtzite
Lattice constant	a = b = 3.28910 Å and c = 5.30682 Å
Molar mass	81.3 g/mol
Density	5.606 g/cm^3
Melting point	2248 K
Bond length	1.977 µm
Energy gap	3.37 eV (direct)
Refractive index	2.008, 2.029
Dielectric constant	$\varepsilon_{\parallel} = 8.75$, $\varepsilon_{\perp} = 3.75$
Effective mass	Electron = 0.24 Hole = 0.59
Exciton binding energy	60 meV
Electron-hole mobility	200 cm^2/V $\cdot$ s
Ionicity	62%
Thermal conductivity	60 W/m $\cdot$ K
Heat capacity	C_p = 9.6 cal/mol $\cdot$ K
Breakdown voltage	5×10^7 V/cm
Heat of crystallization	62 kJ/mol

Table 1.1: Physical Parameters of ZnO

[15]

- Intrinsic Semiconductors (Pure). In these materials, all electrons in the conduction band originate from the valence band. There are no dopant atoms present
- Extrinsic Semiconductors: In contrast, these are intrinsic semiconductors doped with specific impurities, which impart tailored electrical properties optimized for electronic and optoelectronic applications.

Doping is the process of adding small quantities of impurities to a pure semiconductor material to enhance its conductivity. The valence and conduction bands are separated by a bandgap , which electrons can only overcome through external excitation .

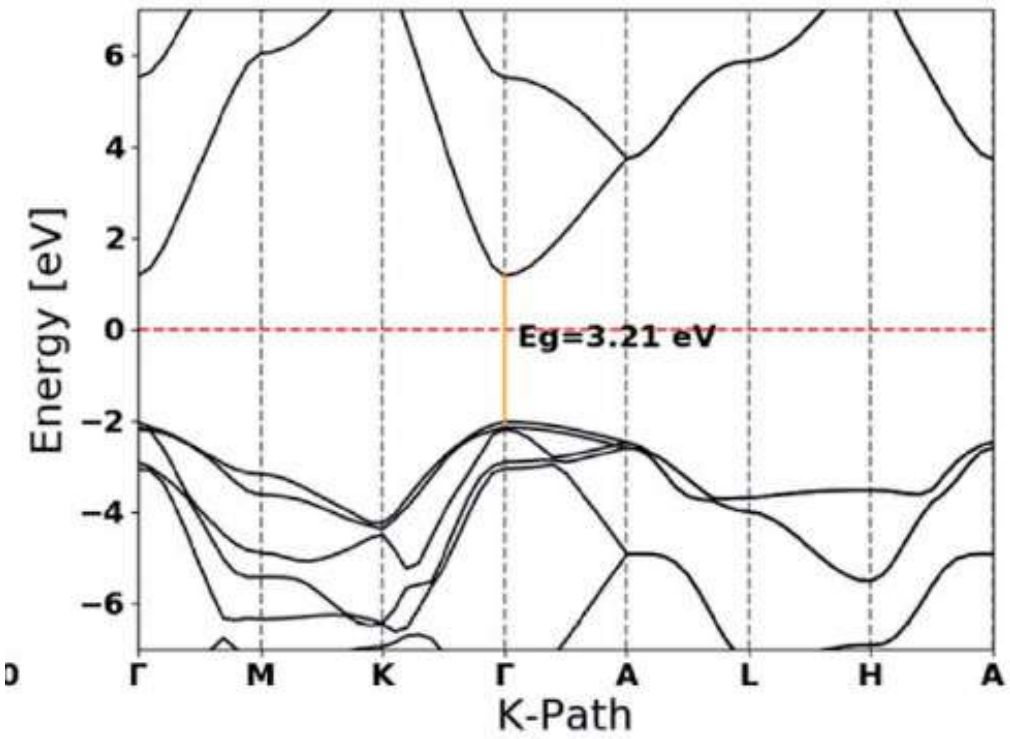


Figure 1.8: Band Structure of ZnO Wurtzite[16]

Doping introduces new donor and acceptor energy levels within the band structure of the material. These levels arise within the bandgap, between the valence and conduction bands [17]. The valence and conduction bands are separated by a bandgap , which electrons can only overcome through external excitation.

Chapter 2

METHODOLOGY

- **The concept of Density Functional Theory (DFT).**
- **Full-Potential Linearized Augmented Plane Wave method (FP-LAPW).**
- **WIEN2k code**

2.1 The equation of Schrödinger and problem of several particles

In order to comprehend the characteristics of condensed matter, it is necessary to examine a system comprised of electrons and nuclei that interact with one another. According to the principles of quantum mechanics, the behavior of this system is dictated by the many-body Schrodinger equation, which encompasses all of the interactions within the system. This equation was first formulated by E. Schrodinger in 1926 [19, 20], and can be expressed in the following manner:

$$\hat{H}\psi = E\psi \tag{2.1.1}$$

Where the Hamiltonian $\hat{H}$ is a set of variables representing multiple physical interactions within the system, including kinetic energy, potential energy, and interactions with electromagnetic fields.

The Hamiltonian function for a solid with N particles is defined as:

$$\hat{H} = \hat{T}_{el} + \hat{V}_{el} + \hat{T}_Z + \hat{V}_Z + \hat{V}_{el-Z} \tag{2.1.2}$$

- $\hat{T}_{el}$: the electron kinetic energy.
- $\hat{V}_{el}$: the electron-electron interaction.
- $\hat{T}_Z$: the nucleus kinetic energy.
- $\hat{V}_Z$ is the interaction nucleus-nucleus.
- $\hat{V}_{el-Z}$ is the interaction between electrons and nucleus.

Then

$$\hat{H} = -\frac{\hbar^2}{2}\sum_n \frac{\nabla^2_{r_i}}{m_{el}} - \frac{\hbar^2}{2}\sum_n \frac{\nabla^2_{R_n}}{M_n} - \frac{1}{4\pi\epsilon_0}\sum_{n,m}\frac{e^2 Z_n}{\mid \vec{R}_n - \vec{r}_m \mid} + \frac{1}{8\pi\epsilon_0}\sum_{n\neq m}\frac{e^2 Z_n Z_m}{\mid \vec{R}_n - \vec{R}_m \mid} + \frac{1}{8\pi\epsilon_0}\sum_{n\neq m}\frac{e^2}{\mid \vec{r}_n - \vec{r}_m \mid} \tag{2.1.3}$$

The Hamiltonian operator, which accounts for the motion and interactions of all atoms within a solid, presents a challenge when applied to systems with multiple bodies. To

address this issue, the equation can be simplified by breaking it down into a set of individual equations that describe the motion of each particle. This process necessitates the development of approximations. The first simplification is achieved by adopting the Born-Oppenheimer approximation [21].

2.1.1 Born-Oppenheimer approximation (1927)

The resolution of the Schrodinger equation in crystal systems is a complex task due to the multitude of interactions depicted in equation (2.1.3). M. Born and J.R. Oppenheimer[21] proposed that nuclei can be considered fixed, while the electrons are much lighter than the nuclei. As a result, the momentum of the nuclei becomes slower. This assumption results in the nuclei having zero kinetic energy ($T_Z = 0$)[22]. Leading to a separation of the electronic and nuclear wave functions, this allows for the independent calculation of the levels of electronic energy and wave functions of a molecule from the nuclei.

The Hamiltonian is reduced as follows:

$$\hat{H} = \hat{T}_{el} + \hat{V}_{el-el} + \hat{V}_{ext} \tag{2.1.4}$$

The wave function of a crystal is influenced by both electrons and nuclei, and can be divided into two components based on their respective contributions (Ψ_{el}, Φ_Z). The kinetic energy of the electron gas in a solid can be described as the energy resulting from the interaction between two electrons, which creates a potential energy represented by $\hat{V}_{el-el}$. The external potential of positively charged nuclei is denoted by $\hat{V}_{ext}$.

$$\Psi(\vec{r}_i; .....; \vec{R}^0_\alpha) = \Psi_{el}(\vec{r}_i; ....; \vec{R}^0_\alpha)\Phi_Z(\vec{R}^0_\alpha) \tag{2.1.5}$$

The wave function of electrons, represented by Ψ_{el}, depends on the positions of the electrons ($\vec{r}_i$, where $i = 1...n$) and the fixed nuclei ($\vec{R}^0_\alpha$). The nuclear wave function is denoted as Φ_Z.

In order to obtain a solution for the Schrodinger equation, a set of fixed nucleus locations is utilized as parameters. The resolution of the equation requires solving a set of equations:

$$\hat{H}_e\psi_{el} = E_{el}\psi_{el} \tag{2.1.6}$$

Then

$$[-i\frac{\hbar^2}{2}\sum_n \frac{\nabla^2_{r_i}}{m_{el}} + \frac{1}{8\pi\epsilon_0}\sum_{n\neq m}\frac{e^2}{\mid \vec{r}_n - \vec{r}_m \mid} - \frac{1}{4\pi\epsilon_0}\sum_{n,m}\frac{e^2 Z_n}{\mid \vec{R}_n - \vec{r}_m \mid}]\psi_{el} = E_{el}\psi_{el} \tag{2.1.7}$$

E_{el} represents the energy of electrons that move in the field created by the fixed nucleus ($E_{el}(R^0_\alpha)$).

It is important to acknowledge that the motion of nuclei is governed by a distinct wave function, denoted as $\Phi_Z(\vec{R}_{1,.....})$. Subsequently, we undertake the task of resolving the given equation:

$$\hat{H}_Z\Phi_Z = E\Phi_Z \tag{2.1.8}$$

$$\hat{H}_Z\Phi_Z = \sum_\alpha(\frac{-\hbar^2\Delta^2_\alpha}{2M_\alpha} + \hat{V}_Z + E_e(..,\vec{R}_1,..))\Phi_Z = E\Phi_Z \tag{2.1.9}$$

The nuclear wave function Φ_Z describes the average value of electron motion.

The Born-Oppenheimer approximation exhibits several notable deficiencies, a few of which are outlined below:

► The Born-Oppenheimer approximation may prove inadequate in cases where electronic and vibrational motions are closely intertwined, despite its assumption to the contrary. This can result in non-adiabatic consequences.

► Due to the potential variability of nuclear coordinates, it cannot be assumed that the electronic wave function will remain constant, which leads to electronic relaxation. This phenomenon is not accounted for by the Born-Oppenheimer approximation.

► The Born-Oppenheimer assumption becomes unreliable when subjected to high pressure or temperatures because it assumes that the nuclei are stationary at their equilibrium positions. However, at such conditions, the nuclei can experience significant displacement.

►The Born-Oppenheimer methodology relies on the concept of isolating the ground state of the electron from its excited states. However, this hypothesis proves inadequate when illustrating electronic states that are significantly elevated.

At this level, there exist multiple approaches to address equation 2.1.5,the initial ones

being the Hartree and Hartree-Fock methods, which rely on the assumption of free electrons [23, 24].

2.1.2 Hartree and Hartree-Fock approximation (1928-1930)

The Hartree approach, based on the independent electron approximation [25, 26], employs the Jellium model to simplify the problem of solving a system of single-particle differential equations. This model assumes that electrons in a material behave like a homogeneous electron gas, thereby simplifying the problem. The Hartree approximation neglects the interactions between electrons and spin states, but it accounts for the mean field potential. The overall wave function is obtained by separating it into the wave functions of individual particles $\psi^i(\vec{r})$:

$$\psi^H(\vec{r}) = \psi^1(\vec{r}_1).\psi^2(\vec{r}_2).\psi^3(\vec{r}_3)....\psi^N(\vec{r}_N) \tag{2.1.10}$$

The equation (2.1.10) mentioned above lacks asymmetry when two electrons are permuted, indicating that these electrons are classified as fermions. As such, the electron spin and Pauli exclusion principle are not disregarded, necessitating the alteration of ψ's sign upon the permutation of two electrons. The total wave function must therefore be asymmetric and expressed in the following format:

$$\psi^H(\vec{r_1}, \vec{r_2}, ..., \vec{r}_N) = -\psi^H(\vec{r_1}, \vec{r_2}, ..., \vec{r}_N) \tag{2.1.11}$$

Hence. Fock suggested adopting a linear combination of independent electron wave functions in a solitary Slater determinant configuration to express the wave function of a system with N electrons [**?**]. This configuration is expressed in the following form [**?**]:

$$\psi^{HF}(\vec{r_1}, \vec{r_2}, ...\vec{r_n}) = \frac{1}{\sqrt{n!}} \begin{vmatrix} \psi^1(\vec{r_1}) & \psi^2(\vec{r_1}) & ... & \psi^N(\vec{r_1}) \\ \psi^1(\vec{r_2}) & \psi^2(\vec{r_2}) & ... & \psi^N(\vec{r_2}) \\ \vdots & \vdots & ... & \vdots \\ \psi^1(\vec{r_n}) & \psi^2(\vec{r_n}) & ... & \psi^N(\vec{r_n}) \end{vmatrix} \tag{2.1.12}$$

Where $\psi^{HF}(\vec{r_i})$: is the one-electron wave function that depends on the local coordination of the electron spin and vector $\vec{r_i}$.

The normalization factor, denoted as $\frac{1}{\sqrt{n!}}$, is used in the context of the determinant of Slater, which exhibits anti-symmetry. Pierre Hohenberg and Walter Kohn's seminal paper on the symmetry principle and exchange effects yielded highly satisfactory results. However, the Hartree-Fock wave function fails to account for the electronic correlation term of the system.

By utilizing the variational method to minimize the Hamiltonian operator, the average electronic energy E_e can be determined:

$$\langle H \rangle = \frac{\langle \psi^{HF} | H | \psi^{HF} \rangle}{\langle \psi^{HF} | \psi^{HF} \rangle} \tag{2.1.13}$$

The field of calculus of variations demonstrates that the wave function $\psi^{HF}(\vec{r})$ for each system must minimize the average energy $\langle H \rangle$. The wave functions are obtained as solutions of a second-order differential equation, which is analogous to Schrödinger's equation for a single particle. In order to account for electronic correlations, several techniques have been developed that surpass the Hartree-Fock method. These techniques rely on density functional theory (DFT) [27–29].

Density Functional Theory (DFT)

The Density Functional Theory (DFT) is a reformulation of the N-body quantum problem that focuses solely on the electron density. The original idea of this theory was developed by Thomas and Fermi in 1927[30, 31]. In their initial work, Thomas and Fermi neglected electron-electron interactions and treated the system as a homogeneous gas, with the kinetic energy being a function of the local density [32]. They did not account for the effects of exchange and correlation between electrons, but Dirac addressed this deficiency in 1930 [33] when he introduced the local exchange approximation [33].

This concept depends on the electronic density and replaces the Schrodinger equation with a set of self-consistent equations. Upon solving these equations, the energy and electron density of the entire system can be obtained:

$$\hat{H} = \sum_{i=1}^{N} \left[-\frac{\hbar^2}{2m} \nabla_i^2 + V_{ex}(\mathbf{r}_i) \right] + \frac{1}{2} \sum i = 1^N \sum_{j=1, j \neq i}^{N} \frac{e^2}{|\mathbf{r}_i - \mathbf{r}_j|} \tag{2.1.14}$$

The Hamiltonian consists of the kinetic energy of the electron and the Coulomb interactions. However, the computational complexity of evaluating this equation for systems with a large number of electrons is a persistent challenge. Density Functional Theory (DFT) has emerged as a valuable tool to address this issue.

In this context, the electronic density ($\rho(\mathbf{r})$) serves as the primary variable for describing the energy of the system. The electronic density functional $E[\rho]$ is used to represent the energy of the system, while the exchange-correlation functional $E_{xc}[\rho]$ relates the electronic density to the external potential V_{ext} and the electron-electron interactions. Consequently, the energy of the system can be expressed as a function of these variables.

$$E_{tot} = T_s[\rho] + \int V_{ext}(\mathbf{r}) \rho(\mathbf{r}) d\mathbf{r} + E_{xc}[\rho] \tag{2.1.15}$$

The functional $T_s[\rho]$ represents the density of kinetic energy for the non-interacting electron gas. By minimizing the total energy with respect to the electronic density, one can determine both the electronic density and the V_{ext}.

The importance of Density Functional Theory (DFT) lies in its relative simplicity compared to Schrodinger's equation. By utilizing the equations developed by Hohenberg[34], Kohn, and Sham[**?**], it becomes possible to solve the self-consistent equations.

2.2 Hohenberg-Kohn theorems

According to the Hohenberg-Kohn theorems. [34], the electron density is the sole determinant of a system's electronic properties.

1. In the context of an electron gas, the HK theorem demonstrates that the system's fundamental state and associated charge density are governed by the external potential acting on these particles. Therefore, the energy functional $E[\rho]$ is expressed using the formula for $\rho(r)$.

$$E[\rho] = \langle \phi | H | \phi \rangle = G[\rho] + \int V_{ex}(r_i) \rho(dr) \tag{2.2.1}$$

The HK universal functional is $G[\rho]$[34, 35], This combines all the variables that are independent of the external potential V_{ex}, including the XC interaction and electron kinetic energy:

$$G[\rho] = \langle\psi|T_e + U_{e-e}|\psi\rangle \tag{2.2.2}$$

2. The minimal functional of the total energy $E[\rho(r)]$, for any multi-particle system, which corresponds to the ground state density[34] is described as:

$$\frac{\delta E[\rho(r)]}{\delta\rho(r)} = 0 \tag{2.2.3}$$

The second theorem, which utilizes the variational principle, aims to calculate the density of the ground state for a given external potential V_{ex}. The objective is to determine the two unknown variables in equation (2.2.2), namely $T_e[\rho]$ and $U_{e-e}[\rho]$. However, the Hohenberg-Kohn theorem does not provide any information regarding the $G[\rho]$ term. Therefore, it becomes necessary to employ approximations that are consistent with the Kohn and Sham[36] equations.

2.3 Kohn-Sham equations

The concept of the Kohn-Sham (KS) method is based on representing a system of N interacting fermions in an external potential V_{ext} as a fictitious system of N non-interacting electrons that move in an effective potential V_{eff} [36, 37]. This approach establishes a direct relationship between the electron density and the energy of the ground state of the non-interacting fermions in the effective potential V_{eff}. Consequently, the electron density functional can be expressed using the following equation [38]:

$$G[\rho(r)] = T[\rho(r)] + U_H[\rho(r)] + V_{xc}[\rho(r)] + V_{ex}[\rho(r)] \tag{2.3.1}$$

Where, T is the kinetic energy of the fictitious system:

- $T[\rho(r)]=\sum_i^N \int \psi_i^*(r)\frac{-\hbar^2\nabla^2}{2m}\ \psi_i(r)$.
- U_H is the Hartree potential: $U_H\ [\rho(r)]=\frac{1}{2}\ \int\ \frac{\rho^{'}(r)}{r-r^{'}}dr$
- V_{xc} is the term that includes the XC effects: $V_{xc}[\rho(r)] = \frac{\delta E_{xc}[\rho(r)]}{\delta\rho(r)}$.

▶ V_{ex} is the external potential.

The solution to the Schrodinger equations is obtained through a set of three separate equations, commonly known as the Kohn-Sham equations [39]:

1. The first equation represents the effective potential:

$$\rho(r) \rightarrow V_{eff}(r) = U_H + V_{xc}(r) + V_{ex}(r) \tag{2.3.2}$$

2. the second equation is the Kohn-Sham approach's Schrodinger equation H^{KS} has the following form:

$$H^{KS}\psi_{i(r)} = (\frac{-\nabla_i^2}{2} + V_{eff})\psi_i(r) = \varepsilon_i^{KS}\psi_i(r) \tag{2.3.3}$$

Where the Kohn-Sham Hamiltonian, the energy eigenvalues ε_i^{KS} $(i = 1, 2, ...N)$, and $\psi_i(r)$ are the specific wave functions of an electron.

3. The third one defines the electronic density:

$$\psi_i(r) \rightarrow \rho(r) = \sum_{i=1}^{N} |\psi_i(r)|^2 \tag{2.3.4}$$

2.4 Resolution of Equations

The resolution of the KS equations involves finding the eigenvalues and eigenfunctions that correspond to the system's fundamental state. This requires solving self consistently [36]. The solution process comprises several stages, starting with an initial assumption for the electronic density. The potential $V_{eff}(r)$ is then calculated using equation (2.3.2) in order to solve equation (2.3.3) for $\psi_i(r)$. This solution provides a new density for equation (2.3.4) in order to update the potential. The updated potential is then used to solve the KS equations again, and the process is repeated until convergence is achieved. At convergence, the electron density and potential reach a self-consistent solution, as depicted in the diagram below (2.1).

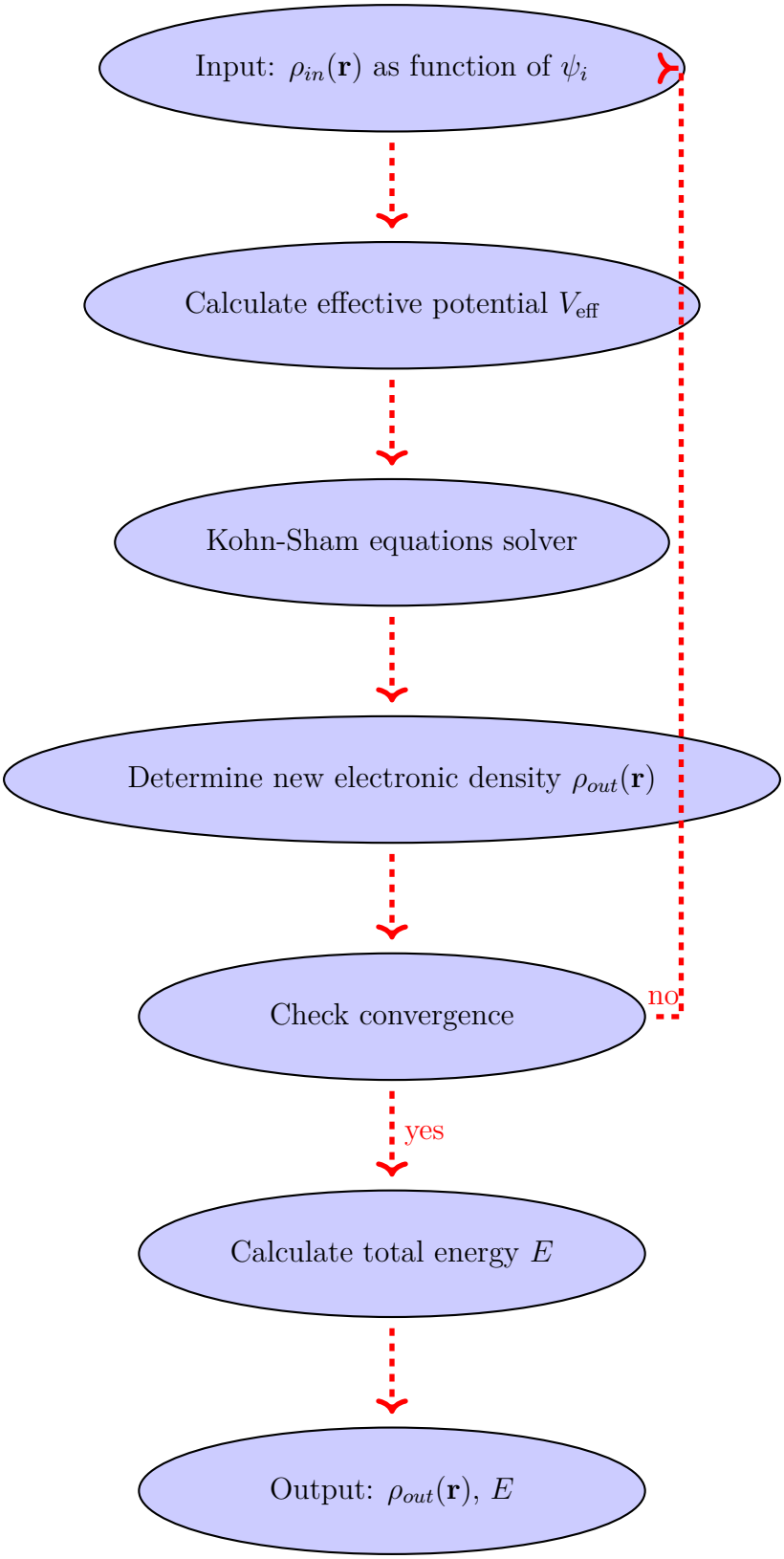


Figure 2.1: The auto-coherent Kohn-Sham diagram.

2.5 The exchange correlation functional

Within the framework of Density Functional Theory (DFT), the exchange-correlation functional plays a crucial role in calculating the total energy. This functional can be divided into two components, namely the exchange functional, which accounts for the electron-electron interaction, and the correlation functional, which describes the correlation between electrons. Despite its significance, the precise form of the exchange-correlation functional, denoted as V_{xc}, remains uncertain. To approximate this functional, various exchange-correlation functionals, such as the local density approximation (LDA), have been proposed. The V_{xc} functional is defined as a function of the electron density, which is based on the concept of Bloch, who postulated that the exchange-correlation could be expressed using the Fermi statistics of a uniform electron gas. [40–45]

2.6 The local density approximation (LDA)

Kohn and Sham formulated the local density approximation (LDA)[36, 44] by postulating that the exchange-correlation energy (E_{xc}) for a given density can be determined by dividing the matter into small volumes with uniform density. Each volume contributes an amount to the overall E_{xc} that is equivalent to that of a volume of the same size containing a homogeneous electron gas with the same total density as the material of origin. As a result, the exchange-correlation energy can be expressed as:

$$E_{xc}^{LDA}[\rho(r)] = \int \rho(r)\epsilon_{xc}[\rho(r)]dr^3 \tag{2.6.1}$$

$\epsilon_{xc}[\rho(r)]$ in a system of homogeneous electrons with the density $\rho(r)$, is the exchange correlation energy contribution made by each electron [46]. Additionally, ϵ_{xc} could potentially be divided into two terms: ϵ_x and ϵ_c, which stand for exchange and correlation, respectively:

$$\epsilon_{xc}^{LDA}[\rho(r)] = \epsilon_x[\rho(r)] + \epsilon_c[\rho(r)] \tag{2.6.2}$$

The correlation term could be writing as: $\epsilon_x[\rho(r)] = -\frac{3}{4\pi r_s}(\frac{9\pi}{4})^{\frac{1}{3}}$: it is coming out of the Dirac exchange functional[33].

The equation (2.6.1) can be readily utilized for the analysis of spin-polarized magnetic systems. Zunger[47] proposed the Local Spin Density Approximation (LSDA) that accounts for both electron density and spin density by estimating them as functions of the exchange-correlation energy at all points in space $\vec{r}$. The spin density, as expressed in the subsequent equation, characterizes the distribution of magnetic moments of electrons in space.

$$E_{xc}^{LSDA}[\rho(r)] = \int (\rho_{\uparrow}(r) + \rho_{\downarrow}(r))\epsilon_{xc}[\rho_{\uparrow}(r), \rho_{\downarrow}(r)]dr^3 \tag{2.6.3}$$

To address the limitations of the local density approximation (LDA), advanced density functionals have been developed that incorporate additional information beyond the local electron density. Perdew (1986) aptly references the Generalized Gradient Theory (GGA) [48], which integrates information on the gradient of the electron density to enhance accuracy.

2.7 Generalized Gradients Approximation(GGA)

The generalized gradient approximation (GGA) is a method that improves upon the local density approximation (LDA) for calculating the exchange-correlation energy in electronic structure calculations. This is achieved by taking into account both the electron density and its gradient, denoted as $\nabla\rho(r)$[48]. The GGA approximation can be expressed mathematically as follows:

$$E_{xc}^{GGAs}[\rho(r)] = \int \rho(r)\epsilon_{xc}[\rho(r)|\nabla\rho(r)|]dr^3 \tag{2.7.1}$$

Where $\epsilon_{xc}[\rho(r)|\nabla\rho(r)|]$[49] represents the exchange-correlation energy per electron in a system of mutually interacted electrons of inhomogeneous density. In other hand, the GGAs[50] approximation with spin polarization could be described in the following equation:

$$E_{xc}^{GGA}[\rho(r)] = \int (\rho_{\uparrow}(r) + \rho_{\downarrow}(r))\epsilon_{xc}[\rho_{\uparrow}(r), \rho_{\downarrow}(r), \nabla_{\uparrow}\rho(r)_{\uparrow}, \nabla_{\downarrow}\rho(r)_{\downarrow}]dr^3 \tag{2.7.2}$$

The GGAs exhibited superior performance compared to LSDA. It is widely acknowledged

that LSDA underestimates the equilibrium lattice constant by 1-3% [50]. In 1986, Perdew et al. developed an estimation technique, known as PW86[51], to address the correlation term. This approach has been documented in literature, including PW91[52] by Perdew and Wang, and PBE[53], a reformulation of PW91 by Perdew, Burke, and Enzerhof[**?**]. These approximations are widely recognized in the field.

2.8 DFT+U approximation

In systems with highly localized d or f shells, the main idea of DFT+U is to introduce a significant intra-site effective Coulomb repulsion among localized electrons. The reason for this is that the LDA and GGA methods are inadequate for predicting the properties of excited states. These methods underestimate the gap between semiconductors and insulators, which is also known as the Hubbard term, U. We utilized a modified version of the DFT+U approach developed by Dudarev et al.[54], which involves combining the DFT approach (LDA or GGA with spin polarization) with a Hubbard Hamiltonian. The Hamiltonian is expressed in a Hamiltonian of a particular form [55]:

$$H = \frac{U}{2} \sum_{m,m',\sigma} \hat{n}_{m\sigma}\hat{n}_{m',\sigma} + \frac{U-J}{2} \sum_{m,m',\sigma} \hat{n}_{m\sigma}\hat{n}_{m',\sigma} \tag{2.8.1}$$

At a particular point, $n_{m\sigma}$ is the operator that determines the number of electrons occupying a state with magnetic quantum number m (m') and spin σ (σ').

The spherically averaged Hubbard parameter, denoted as U [55], measures the energy required to add an additional electron to a specific site. The Stoner exchange parameter can be approximated by J. Meanwhile, U and J are used to describe the intra-site Coulomb repulsion.

Moreover, the role of U and J is not individual, but instead they contribute through their disparity($U_{eff} = U - J$). The value of the U coefficient is typically derived from literature computations or experimental work[54, 56]. In our work, we used this method.

2.9 Spin-Orbit Coupling (SOC)

The inclusion of the spin-orbit (SOC) term, which is often disregarded in the relativistic approximation. This phenomenon arises from the interplay between the spin of an electron and the magnetic field produced by the electron's orbital motion within a fluctuating electrostatic potential surrounding the nucleus. The SOC plays a crucial role in accurately determining the magneto-optical properties of materials that consist of heavy elements or exhibit magnetic behavior[57].

Full-Potential Linearized Augmented Plane Wave method (FP-LAPW)

2.10 The method (APW)

There are several computational codes that are used to solve the band structure problem using DFT. Researchers have developed methods that utilize theoretical concepts known as first-principle methods, including FP-LAPW[58], LMTO[59], PP-PW[60], FPLO[61], and KKR [62]. These methods are commonly employed in density functional theory (DFT) research.

The augmented plane wave (APW)[63] approach, created by Slater in 1937[64–66], was improved upon by the LAPW method, which integrates the Full potential (FP). This method operates on the principle that the potential and wave functions near the atomic nucleus take the form of a "Muffin-Tin" (MT) within a sphere of radius r_α. They exhibit spherical symmetry within this region. Two areas consist of the division of the unit cell: the MT region, and in contrast to the potential and wave functions in the interstitial area among atoms, which may be roughly described as flat, the potential in the MT area exhibits spherical symmetry[67]. Therefore, the wave functions of the crystal are computed using with various basis. Additionally, the Schrodinger equation has radial solutions inside the MT spheres, while outside the sphere region, the solutions are plane

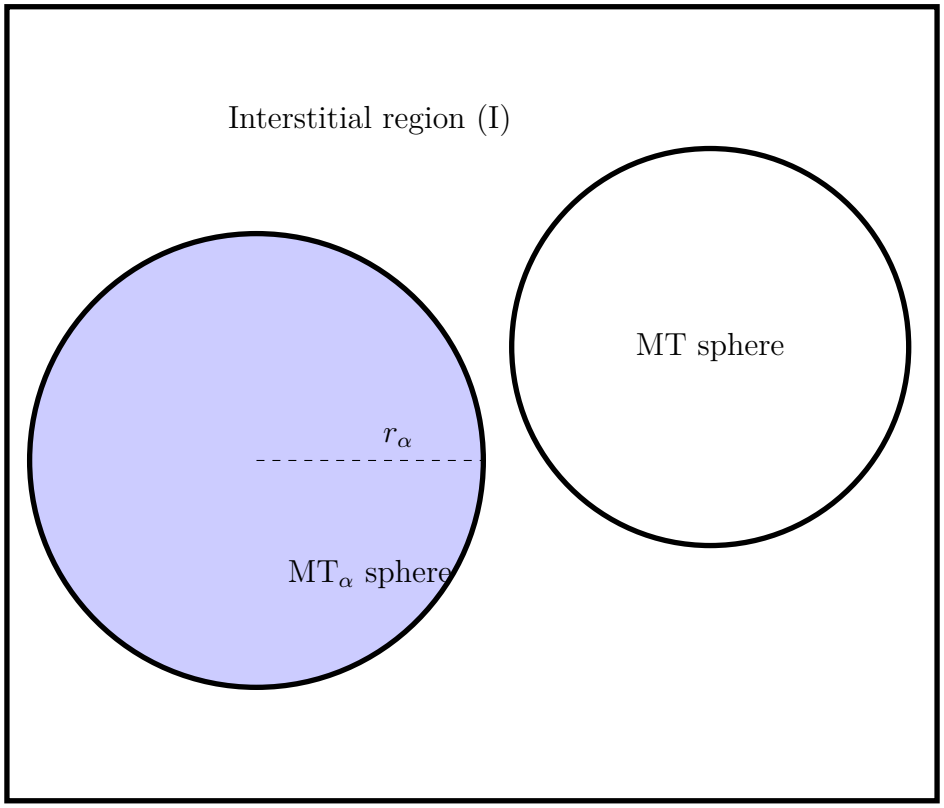


Figure 2.2: Muffin-Tin potential

waves, as illustrated in the figure bellow (2.2).

The crystal potential is constant in the space between the cores. When the wave function $\phi(r)$ is written in the form of[68]:

$$\phi(\vec{r}) = \begin{cases} \frac{1}{\Omega^{\frac{1}{2}}} \sum_{\vec{G}} C_{\vec{G}} e^{i(\vec{G}+\vec{k})\vec{r}}, \ \vec{r} \in I \\ \sum_{lm} A_{lm} U_l(r, E) Y_{lm}(r), \ \vec{r} \in MT_\alpha \end{cases} \tag{2.10.1}$$

The MT_α represents the MT sphere α, $\vec{k}$ is the Bloch vector, r_α is the radius of the vector position of the MT sphere. The symbols $\vec{G}$ and Ω respectively represent the reciprocal lattice vector and the primitive volume. $C_{\vec{G}}$ and A_{lm} are the coefficients in the spherical harmonics Y_{lm}. The variable r represents the position in polar coordinates within the sphere.

The Schrodinger equation solution $U_l(r, E)$ for radial part is given as:

$$\left\{-\frac{d^2}{d^2r} + \frac{l+(l+1)}{r^2} + V_r - E_l\right\} rU_l(r) = 0 \tag{2.10.2}$$

Where $V(r)$ represents the Muffin-Tin (MT) potential and E_l represents the linear energy. The radial functions U_l are orthogonal in every proper state of the core. When the MT sphere reaches its boundaries, this orthogonality vanishes [69], as shown by the following equation:

$$(E_2 - E_1)rU_1U_2 = U_2\frac{d^2U_1}{d^2r} - U_1\frac{d^2U_2}{d^2r} \tag{2.10.3}$$

U_1 and U_2 are the radial solutions corresponding the energies E_1, E_2[68].

To ensure the functionality of the surface of the MT sphere, the coefficients A_{lm} can be generated using the existing C_G plane wave coefficients found in the interstitial region:

$$A_{lm} = \frac{4\pi i^l}{\Omega^{\frac{1}{2}}U_1(\vec{R}_\alpha)}\sum_{\vec{G}} C_{\vec{G}}J_l(|\vec{K}+\vec{g}|\vec{R}_\alpha)Y^*_{lm}(\vec{K}+\vec{G}) \tag{2.10.4}$$

J_l represents the Bessel function of order l [70].

The computation of A_{lm} coefficients is reliant on the imposition of continuity on $U_l(r, E)$ and the corresponding plane wave on the muffin-tin sphere. Slater justified the specific choice of these functions by noting that plane waves provide solutions to the Schrodinger equation if the potential is constant, while radial functions are solutions in a spherical potential when E_l is equal to an eigenvalue. This approximation is highly accurate for materials with cubic face-centered structures, but becomes less satisfactory as the symmetry of the material decreases.

The main problem caused by this method is the discontinuity of the function $\Psi(\vec{r}, E)$ at the surface of the MT sphere. In order to ensure continuity at this boundary, the coefficients A_{ml} must be expanded in terms of the coefficients C_G. In this expansion, if the radial part $U_l(r, E)$ becomes zero for a certain value of E, there will be no continuity. To overcome this, several modifications of the method have been proposed by Koelling and Andersen[71, 72].

2.11 FP-LAPW method

The full potential linearized augmented plane-wave (FP-LAPW) variational expansion approach is used to solve the DFT equations [58, 73]. This method utilizes basis functions that are formed by linearly combining radial functions $U_l(r)Y_{lm}(r)$ and their energy derivatives within the MT spheres[74].

The LAPW method employs plane waves as functions solely within the interstitial region, similar to the APW method[71, 72]. However, within the spheres, the functions are augmented by linear plane waves that offer greater variational freedom. The radial function U_l can be described in terms of its derivative $\dot{U}_l = \frac{dU_l(r,E)}{dE}|_{E=E_l}$, where E_l is a fixed value:

$$\left\{-\frac{d^2}{d^2r} + \frac{l+(l+1)}{r^2} + V_r - E_l\right\} r\dot{U}_l(r) = rU_l(r) \tag{2.11.1}$$

The values and derivatives of plane waves on the boundaries of the sphere in the context of the non-relativistic case correspond to the functions. These plane waves are enhanced and become the LAPW basis functions, also known as LAPWs[68]. Consequently, the wave functions are shown in terms of:

$$\phi(\vec{r}) = \begin{cases} \frac{1}{\Omega^{\frac{1}{2}}} \sum_{\vec{G}} C_{\vec{G}} e^{i(\vec{G}+\vec{k})\vec{r}}, \ \vec{r} \in I \\ \sum_{lm}(A_{lm}U_l(r,E_l) + B_{lm}\dot{U}_l(r,E_0))Y_{lm}(r), \ \vec{r} \in MT_\alpha \end{cases} \tag{2.11.2}$$

The B_{lm} coefficients represent the derivative of energy and are similar to the A_{lm} coefficients. The coefficients A_{lm} and B_{lm} are determined in such a way that each basis function and its derivative are continuous at the interface between Muffin-Tin spheres and the interstitial region.

$$U_l(r,E) = U_l(r,E) + (E-E_l)\dot{U}_l(r,E_l) + O((E-E_l)^2) \tag{2.11.3}$$

The error introduced in the calculation of the wave function and band energy is of the order of $O((E-E_l)^2$ and $(E-E_l)^4$ [72], respectively. However, despite this order of error, the linearly augmented plane waves (LAPW) form a good basis that allows for the

treatment of all valence bands within a large energy range using a single value of E_l. In cases where this is not possible, the energy window can generally be divided into two parts, which is a significant simplification compared to the APW method. In general, if the U_l is null at the surface of the sphere then, its derivative $\dot{U}_l \neq 0$, then the problem of continuity of the wave function at the MT sphere surface does not arise in the LAPW method.

2.12 Modification of FP-LAPW

The primary challenge confronting the LAPW technique pertains to the inadequacy of a single set of E_l to effectively account for all valence bands, particularly in materials that contain 4f orbitals [75, 76]. The situation is commonly referred to as the semi-core state, which indicates an intermediate state that exists between the valence and core states. To address this issue, the initial approach involved dividing the energy levels into multiple windows or developing local orbitals.

2.12.1 Multiple energy windows

In this window-based treatment, a distinction is made between the valence state and the semi-core state, where a set of El is chosen for each window to handle the corresponding states. This entails performing two independent LAPW calculations, albeit with the same potential, as shown in figure bellow (2.3)[77, 78]:

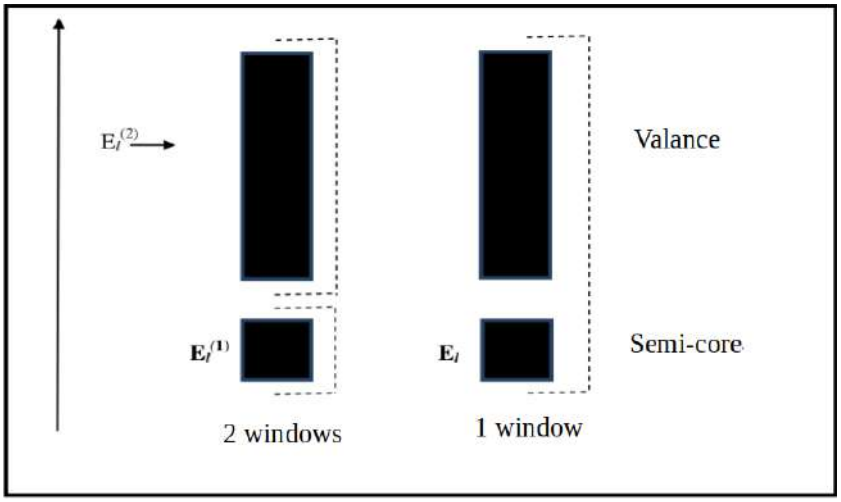


Figure 2.3: exemple of multiple energy windows.

2.12.2 Local orbitals

The LAPW method was devised as a means of obviating the necessity for multiple energy windows by modifying the local orbitals of its basis. The objective of this technique is to address all energy bands using a single energy window, which can be achieved by designating the semi-core state. Various suggestions have been put forward by Takeda et al. [79–81]. Singh [82] has recently proposed a method that involves combining two radial functions with different energies in a linear manner and deriving one of these functions:

$$\phi_{lo}(\vec{r}) = \sum_{lm}(A_{lm}U_l(r', E_l) + B_{lm}\dot{U}_l(r', E_l) + C_{lm}U_l(r, E_l))Y_{lm}(r') \tag{2.12.1}$$

To obtain the coefficients A_{lm}, B_{lm}, and C_{lm}, we need to satisfy two conditions for the function ϕ_{lo}.

2.12.3 The concept of FP-LAPW

In the linearized augmented plane wave with the full potential (FP-LAPW) method[58], no approximations are made for the shape of the potential or charge density. Instead, they are preferably expanded in terms of lattice harmonics within each atomic sphere and Fourier series in the interstitial regions. This ensures the continuity of the potential

at the surface of the muffin-tin sphere and it is developed in the following form:

$$\rho(r) = \begin{cases} \sum_k \rho_k e^{ikr}, \ r > r_\alpha \\ \sum_{lm} \rho_{lm}(r) Y_{lm}(r), \ r < r_\alpha \end{cases} \tag{2.12.2}$$

2.13 WIEN2k code

The package of software called WIEN2k consists of set of programs, is commonly utilized to calculate the properties of matters. Wien2K has advanced features like the ability to perform calculations with spin-orbit coupling and model effects of strong electron correlations using the FP-LAPW method. It is only compatible with UNIX (LINUX) operating systems and was developed in FORTRAN90. It was created at Vienna University of Technology in Austria by Karlheinz Schwarz and Peter Blaha [83] The code was initially made available in 1990 under the name WIEN90, and has subsequently received modifications in the form of WIEN93, WIEN95, WIEN97, and, most recently, WIEN2K [84]. With each successive release, additional features and enhancements were introduced.

2.13.1 Initialization (Computational Detail)

The first stage of initialization is creating an input file named *Case.struct* that provides details about the structure, such as the network type, space group, cell parameters (a, b and c in Bohr or (Å)), and atom positions inside the cell. The next step is to do initialization after inputting the parameters or data of any material into the *structGen* page. Once the *case.struct* file is generated, the initialization can be completed using the "$init - lapw$" command line, which requires starting a number of minimal auxiliary processes that will create inputs for the main programs.[84]:

► **NN:**

the file *case.struct* determines the atomic coordination of specific cell. To make sure the atomic spheres don't overlap, use a separation between the nearest neighbors within a certain distance (usually set to 2). Following that, the distances between these closest neighbors are recorded in a different file called *case.outputnn*.

► **LSTART:** By integrating the atomic densities and figuring out how to handle various orbitals in band structure calculations, the charge density of the crystal is produced. It also needs a cutoff energy level, commonly set at -6.0 Ry, to discriminate between core states and valence states.

► **SYMMETRY:** By utilizing the details available including lattice type and atomic positions, the generation of symmetry operations for the spatial group, corresponding to individual atomic sites, and calculates the matrices representing the corresponding rotation operations.

► **KGEN:** Produce unique mesh of K-points within the irreducible part of the first Brillouin zone (BZ).

► **DSTART:** Create a initial density for the self-consistent cycle (SCF cycle) of the atomic densities overlapped that produced in LSTART.

2.13.2 Self-consistent cycle (SCF)

The following program is for calculating SCF cycle, which is the process lunched and it stops until the solution converges:

► **LAPW0:** Computing the potential as sum of the Coulomb potential V_C and the V_{xc} [84].

► **LAPW1:** responsible for determining the eigenvalues, and eigenvectors, with the results being saved in the *case.vector* file[84].

► **LAPW2:** calculation of the valence charge density, which are made up of the electron densities within each MT sphere[84].

► **LCORE:** calculate core states and densities[84].

► **MIXER:** mixes input and output densities[84].

The diagram below (2.4) shows the steps necessary to process the file.struct using Wien2K code.

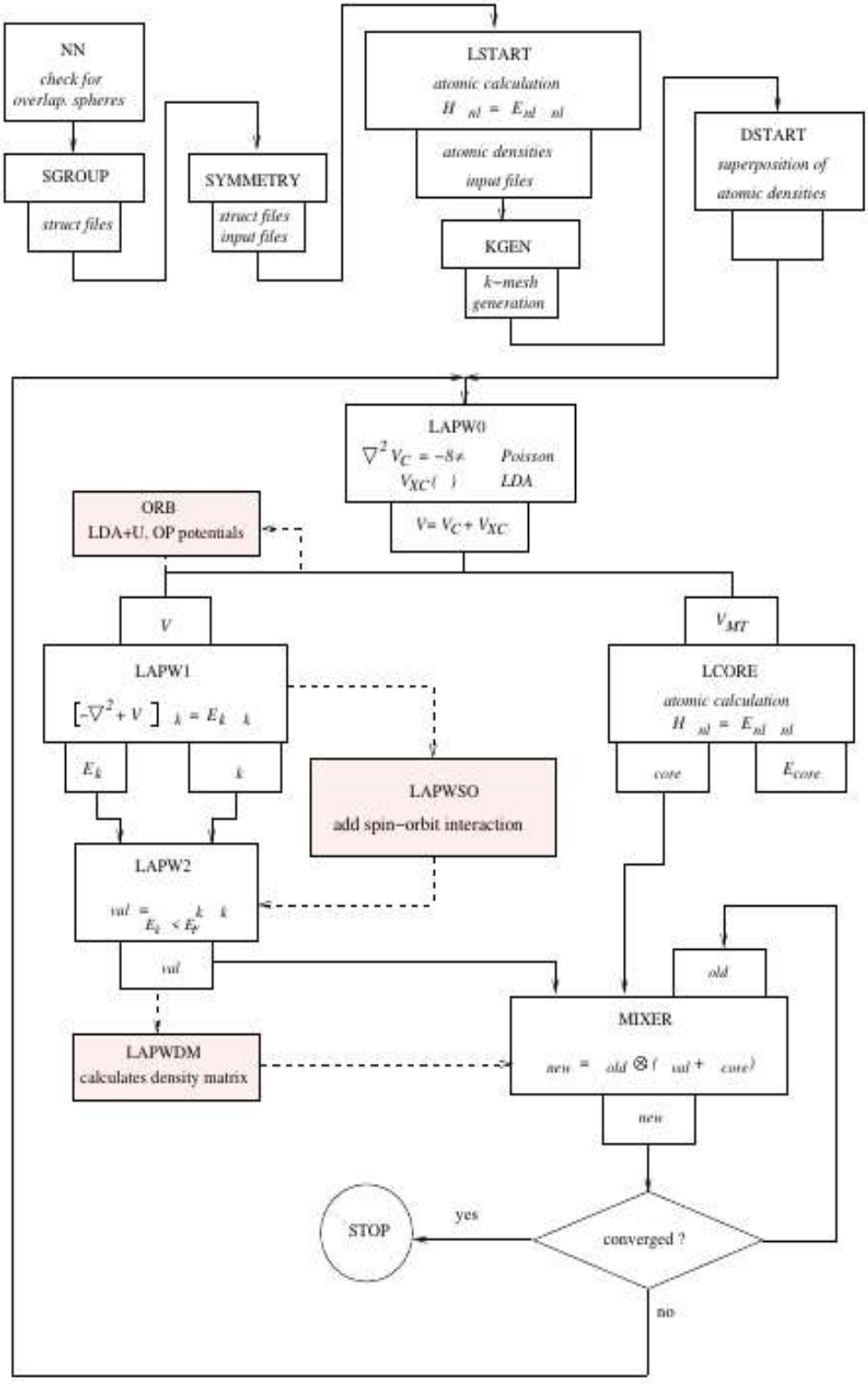


Figure 2.4: Wien2k structure[84].

Chapter 3

Results and Discussion

- **Computational Methodology.**
- **Electronic Properties.**
- **TDOS and Partial DOS.**
- **Magnetic Properties.**

3.1 Introduction

In this chapter, we focus on the investigation of the electronic and magnetic properties of ZnO doped with rare earth (RE) elements. The incorporation of rare earth ions into the ZnO structure is expected to induce significant modifications in the band structure, the density of states, and the overall magnetic behavior of the host material.

The results are analyzed in detail to assess the impact of (RE) doping on the band gap energy and (TDOS , DOS), in order to highlight the key differences and to understand the fundamental mechanisms behind the observed changes.

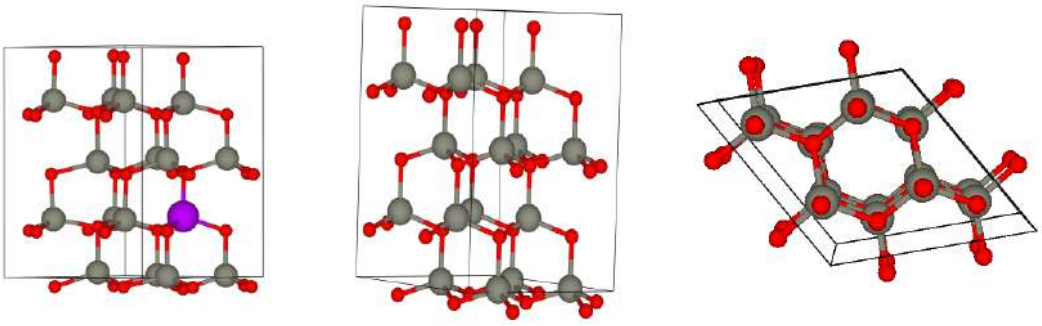
This discussion aims to provide a comprehensive interpretation of how rare earth doping tailors the intrinsic properties of ZnO, offering new opportunities for potential applications in spintronic devices, optoelectronics, and magnetic semiconductors. Whenever possible, the obtained results are compared to previous studies to ensure consistency and to better position the findings within the current scientific context.

3.2 Computational Methodology

The electronic structure calculations were performed using the WIEN2K software package [84], which implements the full-potential linearized augmented plane wave (FP-LAPW) method within the framework of density functional theory (DFT). For the exchange-correlation functional, we employed the generalized gradient approximation (GGA) [**?**]. To achieve accurate bandgap predictions, we additionally employed the Tran-Blaha modified Becke-Johnson potential (TB-mBJ) parameterized by Koller et al. [85], which has demonstrated superior performance for electronic and optical property calculations in solids. Spherical harmonic expansions within non-overlapping muffin-tin (MT) spheres, plane wave basis sets in the interstitial region, energy convergence criterion: 10^{-5} Ry, The radius of the muffin tin spheres was selected as 1.96, 1.60 and 1.96 atomic units for Zn, O and Rare earth (RE) doped element respectively. Plane wave cutoff: $R_{\mathrm{MT}} \times k_{\max} = 7$. For energy convergence we used 4×4×2 k-points in the special irreducible Brillouin zone (BZ) to obtain very good results.

The calculations were performed on the wurtzite, which has a hexagonal structure with space groupe $P6_3mc$ (No. 186), and the atomic position are Zn (2/3, 1/3, 0.500592), O (2/3, 1/3, 0.879718), The supercell constructed a 2×2×2 of the primitive unit cell. The study begins with a ZnO supercell containing a total of 32 atoms, equally distributed between zinc (Zn) and oxygen (O) atoms (16 Zn + 16 O). This structure is constructed by expanding the conventional wurtzite ZnO unit cell (which consists of 2 Zn and 2 O atoms) into a 2×2×2 supercell configuration (Fig. 1). To introduce rare-earth (RE) doping, one Zn atom in the supercell is substituted with an RE atom, maintaining the overall structural integrity while introducing a controlled defect. Given that the supercell contains 16 Zn sites, replacing a single Zn atom with an RE dopant results in a doping concentration of approximately 6.25% atomic.

Figure 3.1: ZnO structure with and without Rare-earth doped and top view image



3.3 Results

3.3.1 Structural parameters

Structural parameters and the crystalline structure of zinc oxide (ZnO) show the effect of doping with rare earth elements (RE) on the crystal structure. ZnO crystallizes in the wurtzite structure, which is considered the most energetically stable compared to the zinc blende and rocksalt structures [86, 87]. The unit cell contains a zinc atoms located at the coordinates (2/3, 1/3,0.500592) and a oxygen atoms located at the coordinates (2/3, 1/3,0.879718) [88, 89].

When ZnO is doped with RE elements such as gadolinium (Gd), europium (Eu), or

terbium (Tb), one of the zinc atoms in the crystal lattice is replaced by a rare earth element, leading to a local distortion in the structure due to the differences in the physical and chemical properties of the elements. This doping induces changes in energy levels within the bandgap [90, 91], affecting optical and magnetic properties. Gd enhances the magnetic properties, making it suitable for spintronic applications, while Eu and Tb improve red and green light emissions, respectively, making them ideal for applications such as display screens and LED devices [92].

Rare earth-doped ZnO structures are created by multiplying the primitive ZnO cell in three directions and replacing one zinc atom with a rare earth atom, as shown in the figure. Before calculating the optical and electrical properties of these doped structures, the structures are optimized by force minimization to obtain the relaxed coordinates. Structural optimization after impurity insertion into ZnO is a crucial step. To achieve this, each structure is relaxed in the X, Y, and Z directions, and the energy of the structure is calculated according to its volume. This energy is then fitted using the Birch-Murnaghan equation of state, from which the optimal structural parameters is deduced [93, 94].

These structural modifications contribute to improving the doped ZnO, making it more efficient for advanced applications such as optical and magnetic devices, sensors, and solar cells. The figure clearly shows the effect of RE doping on the crystal lattice, highlighting the importance of precise control over structural modifications to obtain materials that meet the needs of modern technology [95].

3.3.2 Optimization

The Structural optimization means Improving the crystal structure to achieve the lowest possible total energy of the system or more clearly , finding the optimal geometry which mean the best lattice parameters like cell lengths and the c/a ratio where atoms are in their most stable positions.

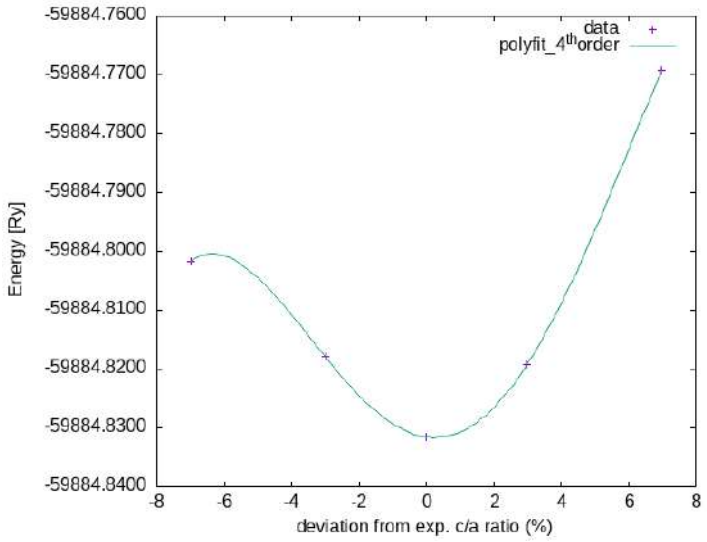
ZnO Optimization

The figure above shows the relationship between the total energy of pure zinc oxide (ZnO), expressed in Rydberg units (Ry), and the relative deviation of the c/a ratio from its experimental value.

The plot reveals a non-linear dependence of the total energy on variations in the c/a lattice parameter ratio. A clear minimum is observed at a deviation close to zero, indicating that the ZnO crystal structure reaches its energetically optimal configuration at or near the experimental c/a ratio. This suggests that the experimental ratio represents the structural equilibrium point of the system.

Furthermore, any deviation—positive or negative—from this optimal ratio leads to a gradual increase in total energy, reflecting a reduction in the structural stability of the material. These findings the sensitivity of the ZnO lattice energy to slight changes in the lattice geometry.

Figure 3.2: Optimization Curve of ZnO



ZnO:Eu Optimization

The graph shows the relationship between the total energy of the ZnO:Eu system and the percentage deviation in the c/a ratio from its experimental value. This structural parameter is critical for stabilizing ZnO's hexagonal lattice and helps identify the most

stable configuration after europium (Eu) doping. This fitting allows determination of the c/a ratio at the energy minimum, representing the most stable doped structure.

Key observations:

- The energy minimum occurs near zero deviation, indicating the optimal c/a ratio remains close to undoped ZnO's experimental value
- Eu doping causes minimal structural distortion, suggesting either:
  - Moderate size mismatch between Eu and Zn
  - Compensating internal strain within the unit cell
- The steep energy increase at positive deviations reveals high sensitivity to c-axis elongation

These results imply that:

- ZnO:Eu maintains stability at nearly the experimental c/a ratio
- The structure is particularly sensitive to expansion along the c-axis
- This sensitivity affects in optical, electronic and magnetic properties

ZnO:Gd Optimization

We performed a structural optimization of Gd-doped ZnO by varying the c/a ratio around its experimental value. The total energy of the system was calculated for each deviation, and a 4th-order polynomial fitting was applied to the data. The resulting energy versus deviation curve exhibits a clear minimum at approximately +3% c/a **ratio**, indicating that the most stable configuration of the Gd-doped ZnO structure corresponds to a slightly elongated lattice along the c-axis.

This shift can be attributed to the incorporation of the larger Gd atom into the ZnO structure, which induces a local distortion and alters the lattice parameters to minimize the system's total energy. The optimized c/a ratio at the energy minimum will be used in subsequent electronic and magnetic property calculations to ensure accurate results.

Figure 3.3: Optimization Curve of $Zn_{15}EuO_{16}$

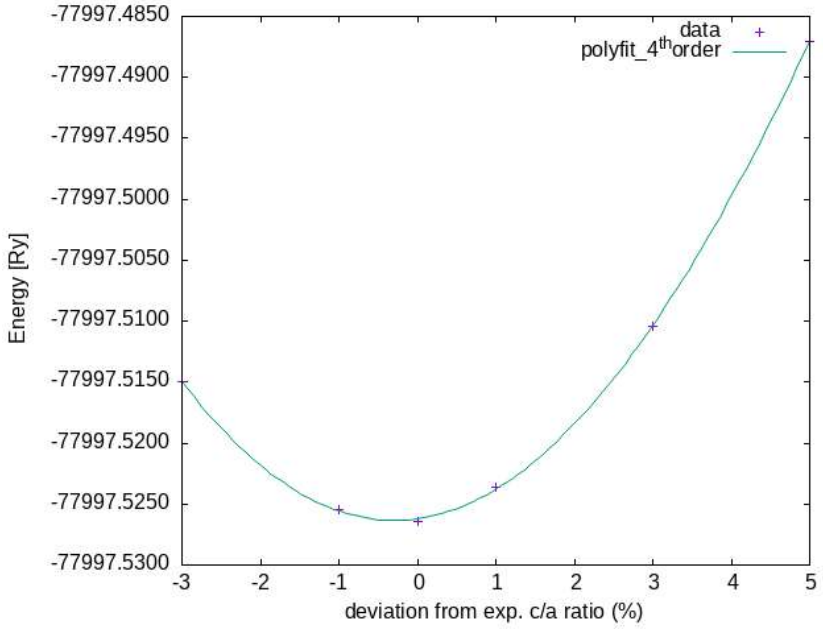
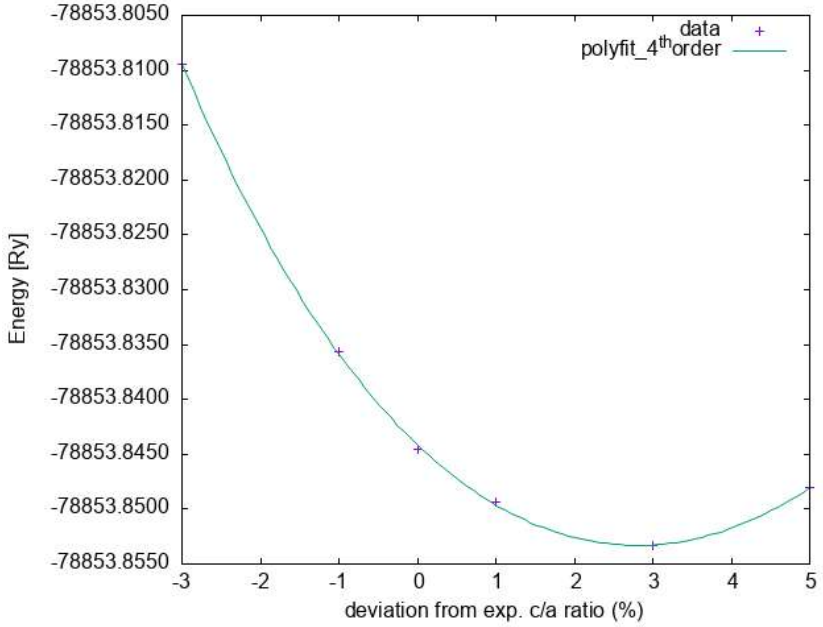


Figure 3.4: Optimization Curve of $Zn_{15}GdO_{16}$



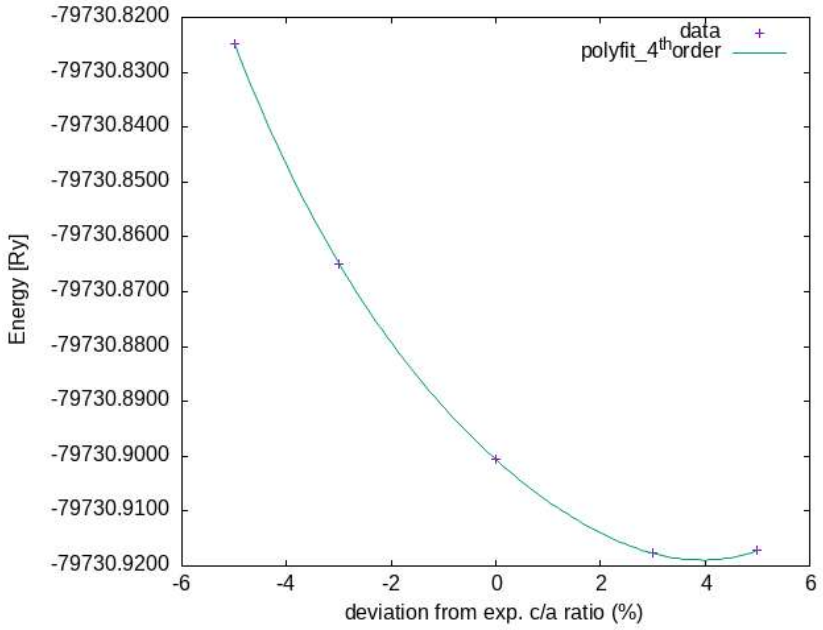
ZnO:Tb Optimization

The c/a ratio is a critical structural parameter in hexagonal crystals like ZnO. Doping with terbium (Tb), which has a larger atomic radius than zinc, alters the atomic arrangement, inducing strain and changing the system's total energy.

The graph shows the relationship between the total energy of the ZnO:Tb system and the percentage deviation from the experimental c/a , with data points calculated using first-principles methods (DFT) and fitted with a fourth-order polynomial. A clear energy minimum appears at a deviation of $\sim +4\%$, indicating that the most stable configuration occurs when the c/a ratio is slightly increased compared to undoped ZnO.

This structural adjustment suggests that doping elongates the crystal along the c-axis or slightly compresses it along the a-axis, highlighting the importance of structural relaxation when introducing dopants. These findings are crucial for optimizing doped ZnO in applications relying on optical, electronic, or magnetic properties, where structural stability directly impacts performance.

Figure 3.5: Optimization Curve of $Zn_{15}TbO_{16}$



The Table3.1 presents a comparison between the theoretical structural parameters (lattice constants a and c, c/a ratio, and supercell volume) obtained in this work and experimental values from the literature for pure and rare earth-doped ZnO (Gd, Eu, Tb). The results show good agreement between our calculations and experimental data for pure ZnO and Gd/Eu-doped systems, while the Tb-doped structure lacks experimental reference data. The tabulated parameters demonstrate how rare earth doping influences the ZnO crystal structure, with variations in lattice constants and unit cell volumes depending on the

Compound	Method	a (Å)	c (Å)	c/a	Vol (Å^3)	Ref.
Pure ZnO	This work	3.23	5.23	1.613	437.8362	/
	Exp.	3.24704	5.19912	—	—	[96]
	Exp.	3.25	5.20	—	—	[97]
	Exp.	3.2501	5.20692	—	—	[98]
Gd	This work	3.263	5.2104	1.681	443.8943	/
	Exp.	3.2735	5.2128	—	—	[100]
Eu	This work	3.235	5.22	1.6171	437.8362	/
	Exp.	3.251	5.209	—	—	[99]
Tb	This work	3.378	5.327	1.5166	477.3157	/
	Exp.	—	—	—	—	—

Table 3.1: Theoretical and experimental structural parameters of rare earth-doped ZnO.

dopant type.

3.3.3 Electronic Structure

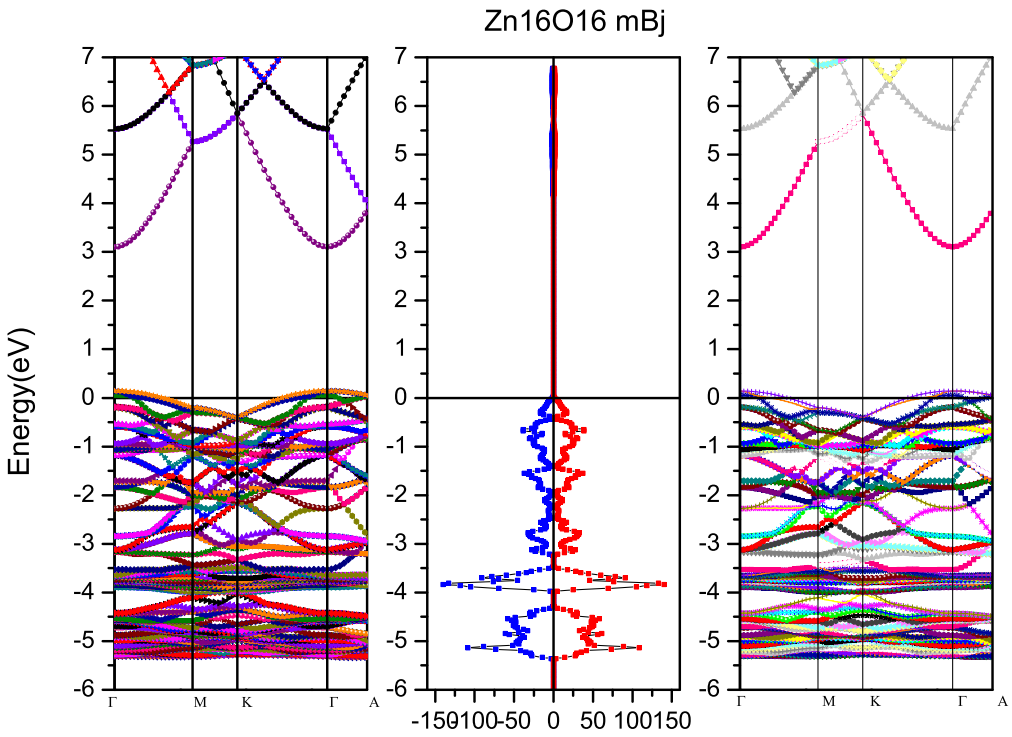
Electronic Structure of Pure ZnO

The figure shows the band structure and total density of states (TDOS) of pure ZnO. The calculations were done using the modified Becke–Johnson (mBJ) potential.

This figure shows that the structure have a direct band gap whose value 3.2 eV which is determined at point Γ close to the experimental value of 3.37 eV. From the band structure, we can see that the valence band is below the Fermi level and the conduction band is above it, meaning there is a clear energy gap. The top of the valence band and the bottom of the conduction band are at the same k-point, which means ZnO has an direct band gap.

Although pure ZnO is not magnetic, both spin-up and spin-down states are shown. The TDOS is almost symmetric, confirming there is no spin polarization, so ZnO is non-magnetic. The energy states below the Fermi level mainly come from Zn-3d and O-2p orbitals. This shows the bonding in ZnO is mostly covalent. These results describe the

Figure 3.6: Total density of state and band structures of $Zn_{16}O_{16}$



electronic structure of pure ZnO and are useful for comparing with doped or defective ZnO systems.

The partial density of states (PDOS) results shows that the valence band can divided into two regions indicate that the Zn-3d orbitals are highly localized in the deep valence band region, specifically from $-8\ eV$ to $-4\ eV$. These orbitals contribute significantly to the lower portion of the valence band, as evidenced by the prominent peaks observed in both the PDOS and the corresponding TDOS within this region. However, these 3d states are far from the Fermi level and therefore have limited direct influence on the material's conduction properties. In the other hand, the O-2p orbitals shows the contribution of the Zn-3d and the O-2p orbitals from around $-6eV$ up to the Fermi level, and they dominate the upper part of the valence band. These orbitals are responsible for the electronic states near the Fermi level Moreover, some hybridization is evident between the Zn-3d and O-2p orbitals, indicating a covalent character in the Zn–O bonding, which significantly shapes the valence band structure and affects both optical and electronic behavior.

By comparing calculations performed without the mBJ potential to those using it, a clear difference in the results can be observed, especially in the estimation of the band gap. Without mBJ, the calculated band gap of zinc oxide is significantly underestimated.

In conclusion when mBJ is applied, the calculated band gap becomes much closer to the experimental value (around 3.3 eV). Moreover, mBJ improves the position of the Zn-3d orbitals and reduces the unrealistic overlap with the O-2p orbitals, leading to a more accurate description of the electronic structure. Therefore, the use of the mBJ functional is essential in theoretical studies aiming to understand the electronic and optical properties of semiconductors.

Electronic Structure for ($Zn_{15}GdO_{16}$):

To study the electronic structure of rare earth-doped ZnO, specifically $Zn_{15}GdO_{16}$, we calculated the band structure, partial density of states (PDOS), and total density of states (TDOS) using Density Functional Theory (DFT). The PBE-GGA functional was initially used, showing an underestimated bandgap. To address this issue, the TB-mBJ potential was employed for more accurate results [94]. The electronic band structure of Gd-doped ZnO maintains a direct bandgap nature at the Γ symmetry point. For the undoped wurtzite structure, ZnO exhibits a calculated bandgap of 3.2 eV (in excellent agreement with the experimental value of 3.3 eV), Gd incorporation induces a notable bandgap reduction to 2.9 eV. This significant decrease of approximately 0.3 eV suggests substantial of the electronic structure through Gd doping.

Additionally, the Fermi level shifts towards the conduction band, confirming the n-type semiconductor nature of the $Zn_{15}GdO_{16}$, as evidenced by the lack of overlap between the conduction and valence bands. The incorporation of Gd introduces localized states within the bandgap, primarily due to the presence of its 4f orbitals [90].

In $Zn_{15}GdO_{16}$, gadolinium doping shifts the valence band to lower energies relative to pure ZnO, highlighting strong interactions between Gd and the ZnO structure. The Total Density of States (TDOS) indicates the presence of occupied states near the Fermi level, significantly influencing the optoelectronic properties of the material [92].

Figure 3.7: PDOS of $Zn_{16}O_{16}$ with mBJ (b) and without mBJ (a)

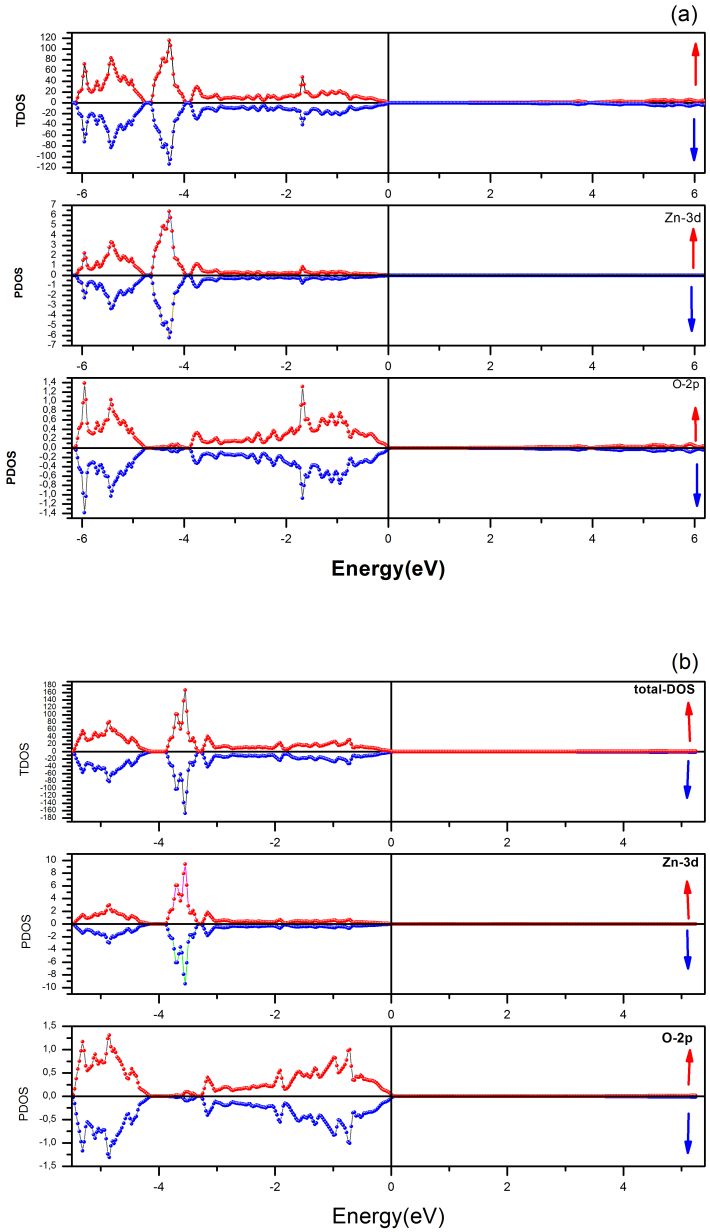
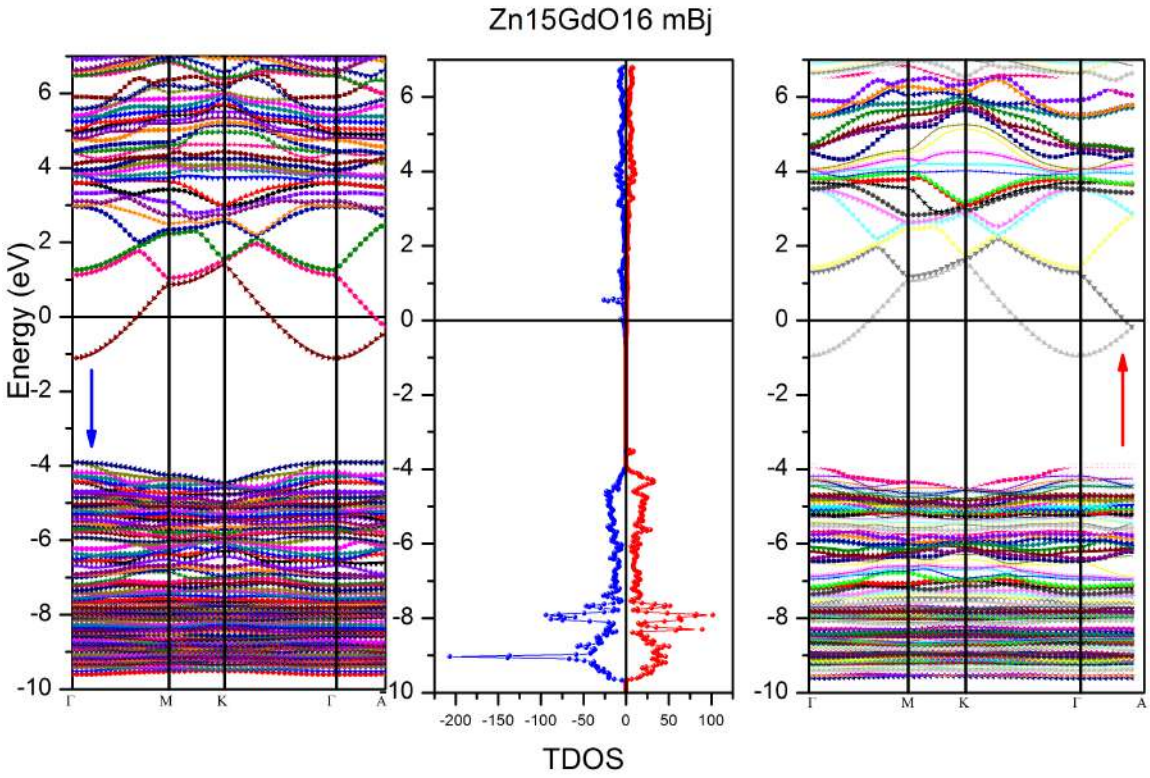


Figure 3.8: Total density of state and band structures of $Zn_{15}GdO_{16}$



The analysis of the density of states (DOS) provides a clear illustration of how Gd doping and the application of mBJ approximations influence the electronic structure of the material. The TDOS and PDOS curves reveal a well-defined bandgap between the valence band maximum and the conduction band minimum, which is a characteristic of semiconductors.

In the first curve (without mBJ), a moderate bandgap is evident, along with a noticeable reduction in the density of states at the Fermi level. The Zn-3d states contribute predominantly at lower energy levels (-8 to -6 eV), signifying their involvement in the inner electronic structure with minimal impact on the bandgap. In contrast, the Gd-4f states show a significant peak near -4 eV and $+0.5$ eV, highlighting their pivotal role in shaping the electronic configuration. The O-2p states contribute primarily at negative energy levels, reflecting the strong bonding of oxygen within the crystal lattice [101].

In the second one (with mBJ), the bandgap is wider and more well-defined, further

emphasizing the material's semiconductor nature. The mBJ approximations refine the representation of Gd-4f states, yielding a sharper and more pronounced peak at $-4\ eV$ and $+0.5\ eV$, signifying an enhanced contribution of these states to the electronic structure. While the contributions of Zn-3d and O-2p remain largely consistent, the improved clarity and precision in the energy distributions reflect the increased accuracy provided by mBJ in modeling the material's electronic properties [102].

In conclusion, the material consistently exhibits semiconductor characteristics, supported by a well-defined bandgap. Gd doping significantly influences the density of states through its f- level contributions, while mBJ approximations enhance the accuracy and precision of electronic structure calculations. These findings underscore the critical role of both Gd and mBJ in tailoring the material's electronic properties and optimizing its performance as a semiconductor [86].

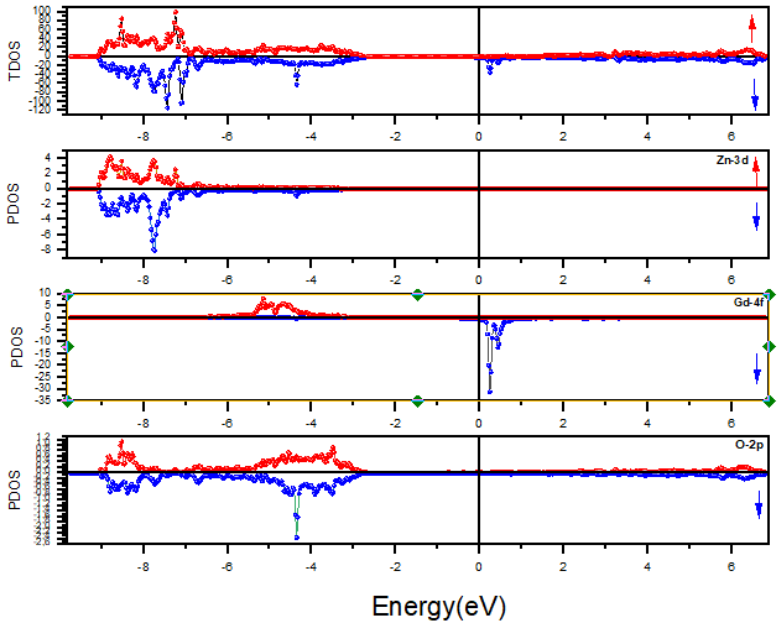
Electronic Structure for $Zn_{16}TbO_{15}$:

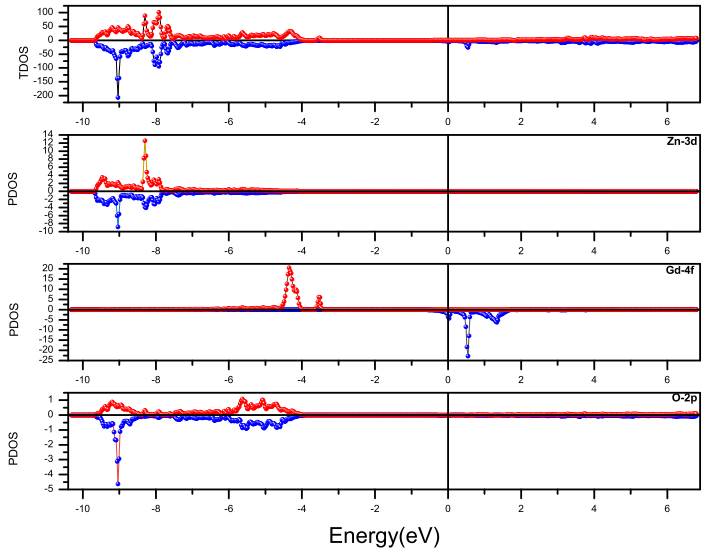
To study the electronic structure of rare earth doped ZnO with Tb , we have calculated the band structure, the partial and total density of states for all the compounds. We have used TB-mBJ potential and we calaculated with and without potential and The results are illustrated in those figures bellow.

This figure show that the structure have a direct band gap , so when we copare with the pure ZnO and the doped we have found that the fermi level is shifted towards the conduction band with no band crossing at the Fermi level and the presence of it close to the conduction band We also observed that the valence states shift to lower energies after doping, which means there is an interaction between the atoms , These more accurately reflects the semiconducting nature of this compound. The band gap is measured from the Fermi level (set at 0 eV) to the highest point of the valence band, showing how doping changes the electronic structure determinated at point Γ is 2.1 eV

Spin-up contains more dense bands below the Fermi level, while in the spin-down direction, one of the bands crosses the Fermi level, indicating a partially half metallic behavior. This difference between the two spin channels reflects the magnetic character of the material.

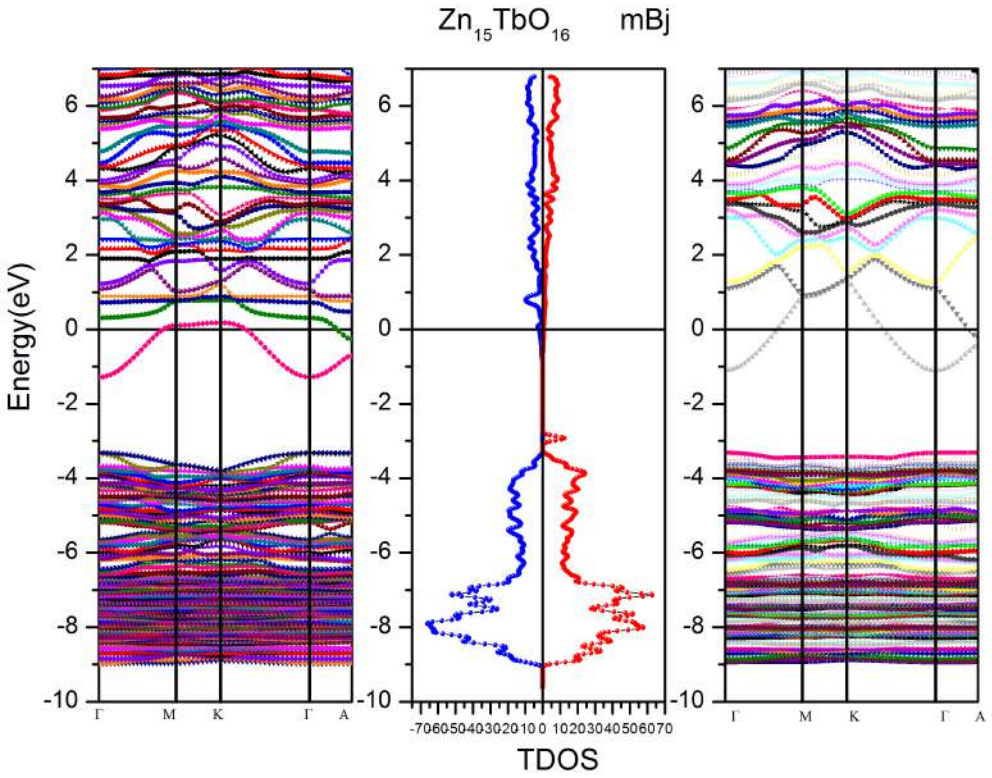
Figure 3.9: PDOS of $Zn_{15}GdO_{16}$ without mBJ (a) and with mBJ (b)





We can see also asymmetry between the spin-up in red and spin-down in blue , which indicates the magnetic nature of the compound. This behavior is primarily due to the presence of the terbium ion (Tb^{3+}), a rare-earth element (lanthanide) that contributes with unpaired 4f electrons. The unpaired electrons establish localized magnetic moments that exchange-couple with the host electron system, resulting in spin-polarized state splitting.

Figure 3.10: Total density of state and band structures of $Zn_{15}TbO_{16}$



To clarify the these bands structures we have calculated the PDOS and the total DOS as it shown is these figures below .

The total and partial density of states (TDOS and PDOS) of Tb-doped ZnO were investigated using two approaches: the standard exchange-correlation functional based on PBE-GGA, and the Modified Becke-Johnson (mBJ) potential, which is known for improving the prediction of band gaps in semiconductors and transition metal oxides.

The PDOS analysis reveals that Tb-4f states in the spin-up are located within the valence band in both cases, but are more clearly and accurately positioned when mBJ is applied, reflecting its effectiveness in describing the localized nature of rare-earth f-orbitals. On the other hand, Zn-3d states remain deeply localized around $-7\ eV$ and show minimal sensitivity to the choice of functional, indicating their weak contribution to the conduction process.

The conduction band made up of the O-2p and Tb-4f(in spin down) states shows the

contribution with orbitals, particularly in the non-mBJ case, suggesting some degree of orbital mixing that could influence the magnetic interactions.

The spin-resolved DOS clearly shows a splitting between spin-up and spin-down channels, indicating the magnetic nature of the system due to the presence of unpaired 4f electrons from Tb^{+3} . This spin polarization is more pronounced with mBJ, especially near the conduction band edge, confirming the magnetic behavior of the compound.

These results shows the role of the mBJ potential in accurately describing the electronic and magnetic properties of doped semiconductors, particularly those involving rare-earth elements

Electronic Structure for $Zn_{15}EuO_{16}$:

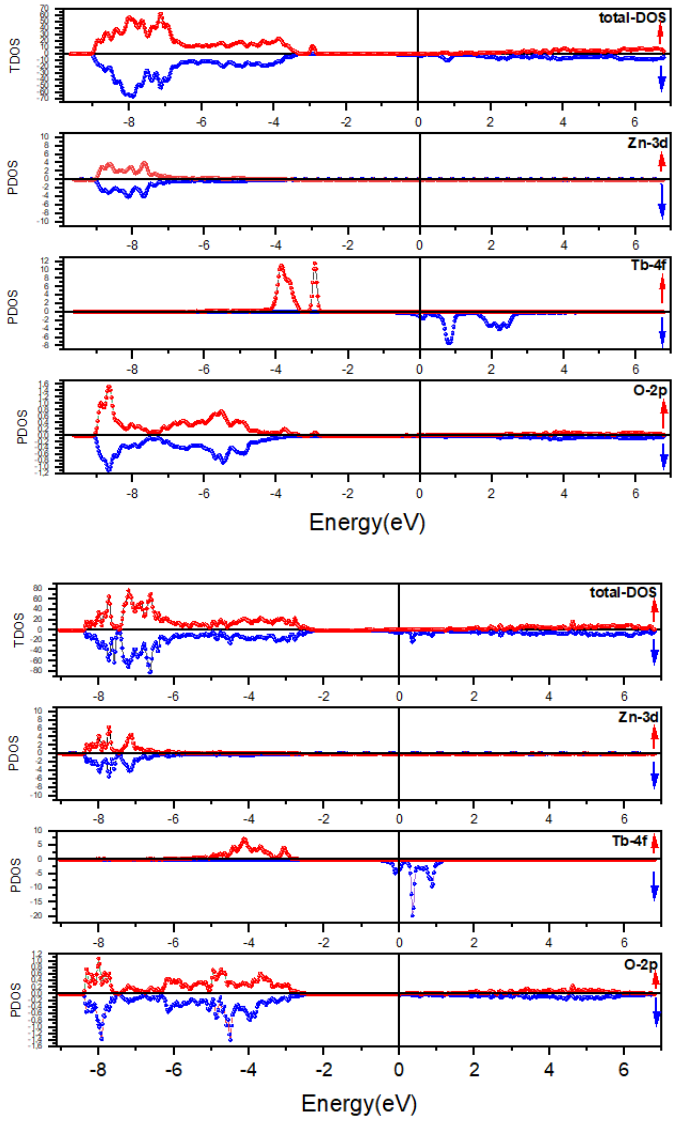
To study the electronic structure of ZnO doped with Eu ($Zn_{15}EuO_{16}$), we calculated the band structure, partial, and total density of states (DOS) using the TB-mBJ potential. Calculations were performed with and without this potential, and the results are illustrated in the figures [86, 94].

The band structure reveals that the compound has a direct band gap at point Γ, with a value of approximately 2.8 eV. Compared to pure ZnO, doping with europium shifts the Fermi level closer to the conduction band without any band crossing, reflecting the semiconducting nature of the material.

Additionally, the valence states shift to lower energy levels due to the interaction between Eu ions and the host lattice atoms, highlighting the significant influence of doping on the electronic structure [103].

The DOS analysis shows a clear asymmetry between spin-up and spin-down states. The spin-up direction exhibits higher band density below the Fermi level, while in the spin-down direction, no bands cross the Fermi level. This indicates a spin-polarized electronic structure but retains the semiconducting character. The magnetic nature of the compound is attributed to the presence of europium Eu^{3+}, a lanthanide with unpaired 4f electrons. These unpaired electrons generate a localized magnetic moment, causing a spin-dependent splitting of electronic states and enhancing the compound's magnetic

Figure 3.11: PDOS of $Zn_{15}TbO_{16}$ with mBJ (a) and without mBJ (b)

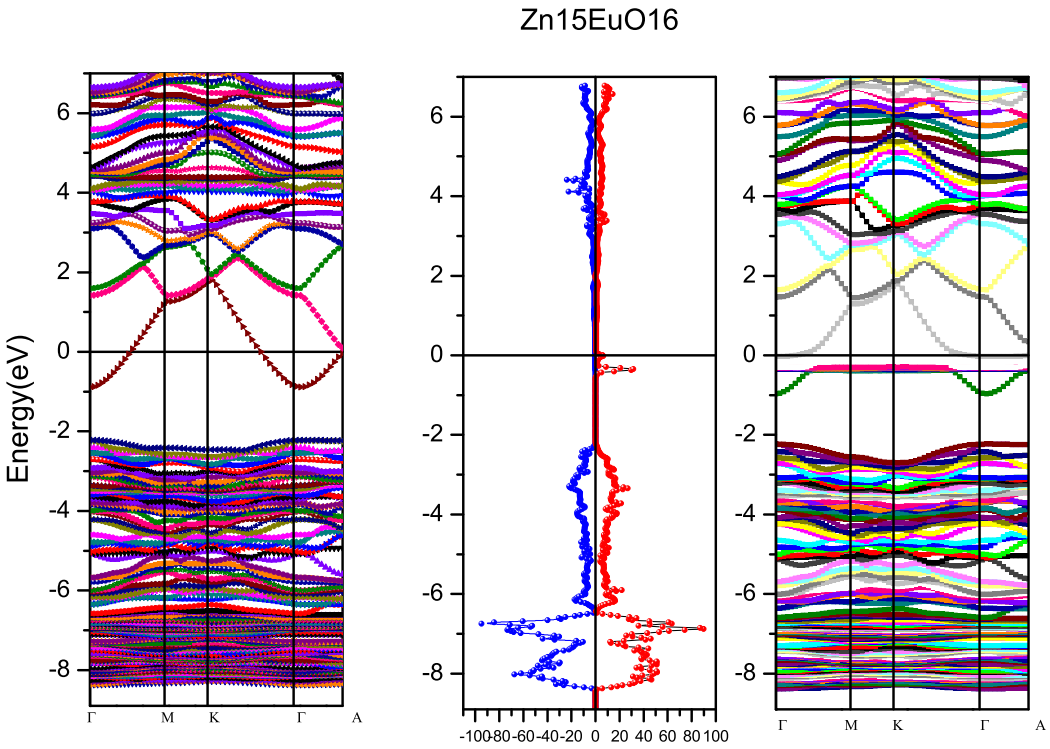


properties [104].

The density of states (DOS) analysis provides insightful evidence on how Eu doping and the implementation of the modified Becke–Johnson (mBJ) potential affect the electronic structure of ZnO. The total (TDOS) and partial density of states (PDOS) plots clearly indicate the presence of a well-defined bandgap, distinguishing the valence band maximum from the conduction band minimum—a signature feature of semiconductors [84, 94].

In the first plot, where mBJ is not applied, the bandgap appears narrower and less distinctly resolved. The Eu-4f states are broader and overlap partially with the valence

Figure 3.12: Total density of state and band structures of $Zn_{15}EuO_{16}$



band, reflecting weaker localization and reduced magnetic influence [90]. Spin polarization is evident, highlighting the magnetic nature introduced by Eu doping. Zn-3d states lie deep in energy (-8 eV), contributing minimally to the bandgap region, while O-2p states dominate the valence band, indicating strong O-Zn bonding characteristics [101].

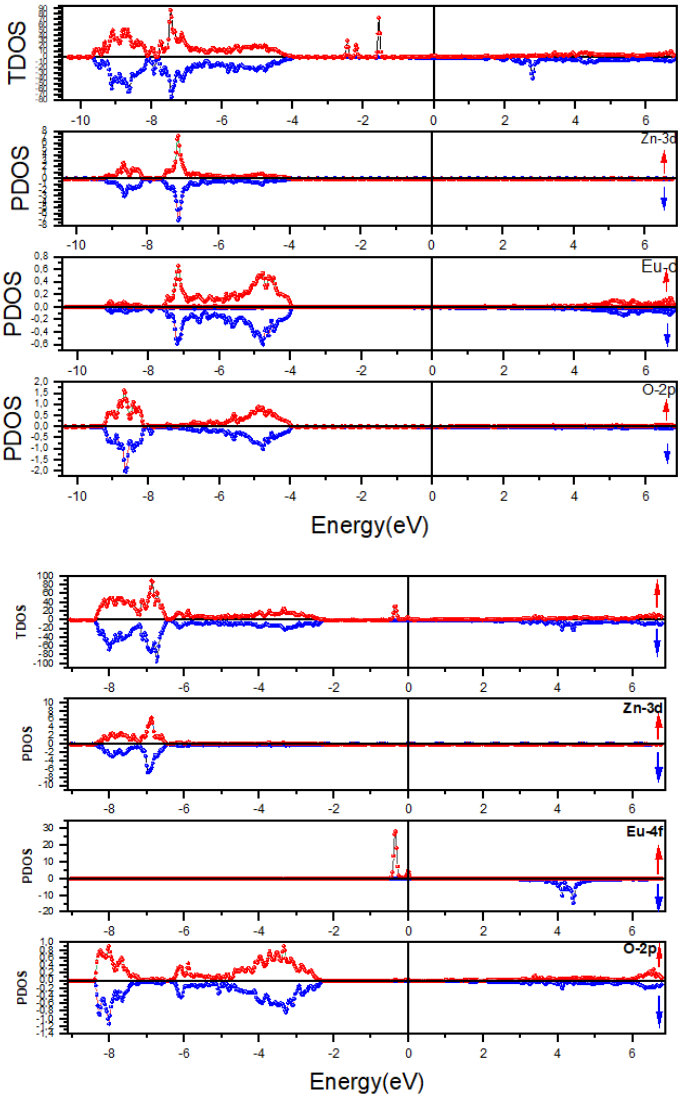
The second plot, calculated using the mBJ potential, shows a more pronounced and wider bandgap, reinforcing the semiconducting identity of the material. Here, the Eu-4f states appear highly localized, forming sharp peaks around $-1\ eV$ and $+4\ eV$. This refined representation suggests an improved treatment of localized electrons by the mBJ functional. Although Zn-3d and O-2p contributions remain relatively unchanged, the energy distribution is more accurate, reflecting enhanced predictive power of mBJ in describing the electronic behavior of strongly correlated systems.

In summary, Eu-doped ZnO retains its semiconductor properties in both scenarios. However, mBJ significantly improves the precision of the electronic structure, particularly in handling localized Eu-4f states. These observations highlight the importance of both Eu incorporation and mBJ corrections in accurately capturing the material's electronic and magnetic characteristics, which are critical for applications in spintronics and optoelectronics [90, 102].

Table 3.2: Comparison of band gaps (in eV) for pure and RE-doped ZnO

Compound	**Method**	**Gap (eV)**	**Reference**
Pure ZnO	This work (DFT)	3.2	–
	Experimental	3.37	[105]
ZnO:Gd	This work (DFT)	2.9	–
	Experimental	3.07	[106]
ZnO:Tb	This work (DFT)	2.1	–
	Theoretical	2.3	[107]
ZnO:Eu	This work (DFT)	2.8	–
	Experimental	3.27	[108]

Figure 3.13: PDOS of $Zn_{15}EuO_{16}$ with mBJ (a) and without mBJ (b)



3.3.4 Magnetic properties

In this study, we investigated the magnetism of RE-doped ZnO using spin-polarized calculations. Pure ZnO exhibits a magnetic moment of $0\mu_B$, with symmetrical spin-up and spin-down density of states (Fig. 3.5), confirming its non-magnetic nature. Upon doping, the total magnetic moments change significantly:

- **Gd-doped ZnO** shows the highest moment (6.95 μ_B in this work vs. 7.00 μ_B in Hachimi et al.), consistent with Gd's half-filled $4f^7$ configuration, which maximizes

Table 3.3: Comparison of spin magnetic moments (in μ_B) for RE-doped ZnO compounds from this work and Hachimi et al. (2014)[107]

Compound	**Total moment**	**RE Moment in ZnO**	**Hachimi et al.**	**Origin**
ZnO	0	0	0	Non-magnetic
ZnO:Eu	5.37	5.88	6.00	Eu $4f^6$
ZnO:Gd	6.95	6.79	7.00	Gd $4f^7$ (Hund's max)
ZnO:Tb	5.70	5.65	6.00	Tb $4f^8$

the moment according to Hund's rules.

- **Eu and Tb-doped ZnO** exhibit slightly lower moments (5.37 μ_B and 5.70 μ_B here) compared to Hachimi et al. (6.00 μ_B for both), likely due to differences in computational parameters or dopant positioning.

The magnetic moment in the cell includes contributions from all atoms, while the sphere moment reflects only the dopant's local environment. For Gd, the cell moment exceeds the sphere moment due to significant polarization of neighboring O ($2p$) and Zn ($3d$) orbitals. In contrast, Tb's closer cell/sphere values suggest more localized magnetism.

The DOS and PDOS confirm that the RE $4f$ orbitals dominate the magnetic behavior, with minor contributions from O $2p$ and Zn $3d$ states [107].

Conclusion

This chapter presented a comprehensive investigation into the structural, electronic, and magnetic properties of pure and rare earth (RE)-doped ZnO, focusing on the effects of doping with gadolinium (Gd), europium (Eu), and terbium (Tb). The study employed advanced computational methodologies, including density functional theory (DFT) with the Wien2k software package, and utilized the Tran-Blaha modified Becke-Johnson (TB-mBJ) potential to achieve accurate predictions of electronic properties.

3.3.5 Structural Modifications:

- Rare earth doping induced local distortions in the ZnO lattice due to differences in atomic radii and chemical properties.
- Structural optimization revealed that the c/a ratio remained close to the experimental value for Eu-doped ZnO, while Tb doping caused a slight elongation along the c-axis, reflecting the system's sensitivity to strain.

3.3.6 Electronic Properties:

- Pure ZnO exhibited a direct bandgap of $3.2\,eV$ (close to the experimental value of $3.37\,eV$), with the valence band dominated by Zn-3d and O-2p orbitals.
- RE doping introduced localized states within the bandgap, primarily from the 4f orbitals of Gd and Tb, which altered the electronic structure. The Fermi level shifted towards the conduction band, confirming n-type semiconductor behavior.
- The TB-mBJ potential significantly improved the accuracy of bandgap calculations, reducing unrealistic overlaps between orbitals and providing a clearer description of the electronic structure.

3.3.7 Magnetic Properties:

- Gd and Tb doping introduced magnetic moments due to their unpaired 4f electrons, leading to spin polarization and asymmetry in the density of states (DOS).
- Tb-doped ZnO exhibited partially half-metallic behavior, with spin-dependent splitting of electronic states, making it promising for spintronic applications.

3.3.8 Comparative Analysis:

- The study highlighted the distinct effects of different RE dopants: Gd enhanced magnetic properties, Eu showed minimal structural distortion, and Tb induced

significant electronic and magnetic modifications.

These results underscore the potential of RE-doped ZnO for advanced applications in optoelectronics, spintronics, and magnetic semiconductors. The insights gained from this work provide a foundation for further experimental and theoretical studies aimed at tailoring ZnO-based materials for specific technological needs. Future research could explore higher doping concentrations, additional RE elements, or the combined effects of multiple dopants to further optimize material performance.

General Conclusion

General Conclusion

This master's thesis has presented a comprehensive theoretical investigation into the influence of rare-earth (RE) metal doping on the electronic and magnetic properties of zinc oxide (ZnO) semiconductors. Using first-principles calculations based on Density Functional Theory (DFT) with the WIEN2k code, we systematically examined the structural, electronic, and magnetic modifications induced by gadolinium (Gd), terbium (Tb), and europium (Eu) doping in the ZnO structure.

Our structural analysis revealed that RE doping induces local distortions in the ZnO lattice, with the extent of distortion varying according to the ionic radius of the dopant. The optimization studies demonstrated that while europium doping maintains the c/a ratio close to that of pure ZnO, terbium doping causes significant elongation along the c-axis, reflecting the system's sensitivity to strain effects. These structural modifications were quantitatively characterized through lattice parameter calculations and compared with available experimental data.

The electronic structure calculations, performed using the modified Becke-Johnson (TB-mBJ) potential to overcome the band gap underestimation problem of standard DFT, showed that all RE dopants introduce localized states within the band gap, primarily originating from their 4f orbitals. The Fermi level shifts toward the conduction band in all doped systems, confirming n-type semiconductor behavior. Notably, the band gap values varied with different dopants, with Gd-doped ZnO exhibiting the largest gap (2.9 eV) among the studied systems.

The magnetic properties analysis revealed that Gd and Tb doping induces significant magnetic moments due to their unpaired 4f electrons, leading to clear spin polarization and asymmetry in the density of states. Particularly interesting was the partially half-metallic behavior observed in Tb-doped ZnO, which suggests promising potential for spintronic applications. Europium doping, while maintaining the semiconducting character, also showed measurable magnetic effects through spin-polarized electronic states.

The comparative analysis of different RE dopants highlighted their distinct influences:

- Gadolinium (Gd) proved most effective in enhancing magnetic properties while maintaining good structural stability
- Terbium (Tb) induced the most significant electronic structure modifications and showed potential for half-metallic behavior
- Europium (Eu) caused minimal structural distortion while still introducing useful electronic and magnetic modifications

These theoretical findings provide valuable insights for the experimental development of RE-doped ZnO materials for advanced applications in optoelectronics, spintronics, and magneto-optic devices. The demonstrated ability to tailor ZnO's properties through selective RE doping opens new possibilities for designing multifunctional semiconductor materials. Future work could explore higher doping concentrations, combinations of different RE elements, or the effects of codoping with other elements to further optimize the material properties for specific technological applications.

This study contributes to the fundamental understanding of rare-earth doping in semiconductors and provides a theoretical framework that can guide experimental efforts in developing ZnO-based functional materials for emerging technologies.

Bibliography

[1] S. M. Sze, *Physics of Semiconductor Devices*, 3rd ed. (Wiley-Interscience, New York, 2006).

[2] B. G. Streetman, *Solid State Electronic Devices*, 6th ed. (Prentice Hall, Upper Saddle River, NJ, 2006).

[3] R. F. Pierret, *Semiconductor Device Fundamentals* (Addison-Wesley, Boston, 1996).

[4] O. Madelung, *Semiconductors: Data Handbook*, 3rd ed. (Springer, Berlin, 2004).

[5] P. Y. Yu and M. Cardona, *Fundamentals of Semiconductors: Physics and Materials Properties*, 4th ed. (Springer, Berlin, 2010).

[6] N. W. Ashcroft and N. D. Mermin, *Solid State Physics* (Holt, Rinehart and Winston, New York, 1976).

[7] F. Mohtaram, A. Edrisy, and J. L. Lan, "Electrospun ZnO nanofiber interlayers for enhanced performance of organic photovoltaic devices," *Sol. Energy* **197**, 1–10 (2020).

[8] Fox, Mark. *Optical Properties of Solids.* Oxford University Press, 2001, p. 356.

[9] F. Dagognet, *Tableaux et langages de la chimie: Essai sur la représentation* (Champ Vallon, Paris, 2002).

[10] E. Arras, "Étude théorique de la structure et de la stabilité des alliages GeMn dans le cadre de la spintronique," Ph.D. thesis, Université Paris-Saclay, 2010.

[11] M. Samira, "Étude des propriétés structurales et magnétiques de semi-conducteur magnétique GeMn," Ph.D. thesis, Université Abou Bakr Belkaid, Tlemcen, 2012.

[12] J. Cibert and D. Ferrand, "Ferromagnétisme contrôlé par les porteurs dans les semi-conducteurs magnétiques," *J. Phys. (Paris)* (unpublished).

[13] N. F. Mott, "Conduction in non-crystalline materials," *Proc. R. Soc. Lond. A* **156**, 368–382 (1936).

[14] Ü. Özgür, Ya. I. Alivov, C. Liu, A. Teke, M. A. Reshchikov, S. Doğan, V. Avrutin, S.-J. Cho, and H. Morkoç, "A comprehensive review of ZnO materials and devices," *J. Appl. Phys.* **98**, 041301 (2005).

[15] Z. L. Wang, "Design of solution-grown ZnO nanostructures," in *Towards Functional Nanostructures*, edited by G. A. Ozin and A. C. Arsenault (Springer, Berlin, 2008), Vol. 7, pp. 325–368.

[16] Davis, K.; Yarbrough, R.; Froeschle, M.; White, J.; Rathnayake, H. "Band gap engineered zinc oxide nanostructures via a sol–gel synthesis of solvent driven shape-controlled crystal growth."*RSC Adv.* **2019**, *9*(26), 14638–14648.

[17] S. Benramache, "Élaboration et caractérisation des couches minces de ZnO dopées cobalt et indium," Ph.D. thesis, Université de Biskra, 2012.

[18] N. Chahmat, "Traitement de l'oxyde de Zinc et étude de ses propriétés physicochimiques superficielles," Ph.D. thesis, Université Badji Mokhtar, Annaba, 2014.

[19] Y. Tsutsumi, "Schrodinger equation," *Funkcial. Ekvac.* **30**, 115–125 (1987).

[20] E. Schrödinger, "An undulatory theory of the mechanics of atoms and molecules," *Phys. Rev.* **28**, 1049–1070 (1926).

[21] M. Born and R. Oppenheimer, "Zur Quantentheorie der Molekeln," *Ann. Phys.* **389**, 457–484 (1927).

[22] M. Huber, "Zur Theorie der Berührung fester elastischer Körper," *Ann. Phys.* **319**, 153–163 (1904).

[23] D. R. Hartree, "Representation of the Exchange Terms in Fock's Equations by a Quasi-Potential," *Phys. Rev.* **109**, 840–841 (1958).

[24] V. Fock, "Näherungsmethode zur Lösung des quantenmechanischen Mehrkörperproblems," *Z. Phys.* **61**, 126–148 (1930).

[25] D. R. Hartree, "The Wave Mechanics of an Atom with a Non-Coulomb Central Field. Part I. Theory and Methods," *Math. Proc. Cambridge Philos. Soc.* **24**, 89–110 (1928).

[26] N. D. Lang and W. Kohn, "Theory of Metal Surfaces: Charge Density and Surface Energy," *Phys. Rev. B* **1**, 4555–4568 (1970).

[27] H. Chermette, "Density functional theory: A powerful tool for theoretical studies in coordination chemistry," *Coord. Chem. Rev.* **178-180**, 699–721 (1998).

[28] H. Paulsen and A. X. Trautwein, "Density Functional Theory Calculations for Spin Crossover Complexes," in *Spin Crossover in Transition Metal Compounds III*, edited by P. Gütlich and H. A. Goodwin (Springer, Berlin, 2004), pp. 197–219.

[29] J. N. Harvey, "DFT Computation of Relative Spin-State Energetics of Transition Metal Compounds," in *Principles and Applications of Density Functional Theory in Inorganic Chemistry I*, edited by D. M. P. Mingos (Springer, Berlin, 2004), pp. 151–184.

[30] L. H. Thomas, "The Calculation of Atomic Fields," *Math. Proc. Cambridge Philos. Soc.* **23**, 542–548 (1927).

[31] E. Fermi, "Un metodo statistico per la determinazione di alcune priorieta dell'atomo," *Rend. Accad. Naz. Lincei* **6**, 602–607 (1927).

[32] R. G. Parr and W. Yang, *Density-Functional Theory of Atoms and Molecules* (Oxford University Press, New York, 1995).

[33] P. A. M. Dirac, "Note on Exchange Phenomena in the Thomas Atom," *Math. Proc. Cambridge Philos. Soc.* **26**, 376–385 (1930).

[34] P. Hohenberg and W. Kohn, "Inhomogeneous Electron Gas," *Phys. Rev.* **136**, B864–B871 (1964).

[35] P. R. Antoniewicz and L. Kleinman, "Kohn-Sham Exchange Potential Exact to First Order in ρ," *Phys. Rev. B* **31**, 6779–6781 (1985).

[36] W. Kohn and L. J. Sham, "Self-Consistent Equations Including Exchange and Correlation Effects," *Phys. Rev.* **140**, A1133–A1138 (1965).

[37] R. A. Harris, "Induction and Dispersion Forces in the Electron Gas Theory of Interacting Closed Shell Systems," *J. Chem. Phys.* **81**, 2403–2405 (1984).

[38] J. Harris and R. O. Jones, "The Surface Energy of a Bounded Electron Gas," *J. Phys. F: Met. Phys.* **4**, 1170–1186 (1974).

[39] W. Kohn, "Density Functional and Density Matrix Method Scaling Linearly with the Number of Atoms," *Phys. Rev. Lett.* **76**, 3168–3171 (1996).

[40] M. Ernzerhof and G. E. Scuseria, "Assessment of the Perdew-Burke-Ernzerhof Exchange-Correlation Functional," *J. Chem. Phys.* **110**, 5029–5036 (1999).

[41] O. Gunnarsson and B. I. Lundqvist, "Exchange and Correlation in Atoms, Molecules, and Solids by the Spin-Density-Functional Formalism," *Phys. Rev. B* **13**, 4274–4298 (1976).

[42] C.-O. Almbladh and A. C. Pedroza, "Density-Functional Exchange-Correlation Potentials and Orbital Eigenvalues for Light Atoms," *Phys. Rev. A* **29**, 2322–2330 (1984).

[43] A. Savin, H. Stoll, and H. Preuss, "An Application of Correlation Energy Density Functionals to Atoms and Molecules," *Theor. Chim. Acta* **70**, 407–419 (1986).

[44] A. Van de Walle and G. Ceder, "Correcting Overbinding in Local-Density-Approximation Calculations," *Phys. Rev. B* **59**, 14992–15001 (1999).

[45] N. W. Ashcroft and N. D. Mermin, *Solid State Physics*, 2nd ed. (Cengage Learning, Boston, 2022).

[46] J. P. Perdew, E. R. McMullen, and A. Zunger, "Density-Functional Theory of the Correlation Energy in Atoms and Ions," *Phys. Rev. A* **23**, 2785–2789 (1981).

[47] A. Zunger, J. P. Perdew, and G. L. Oliver, "A Self-Interaction Corrected Approach to Many-Electron Systems," *Solid State Commun.* **34**, 933–936 (1980).

[48] J. P. Perdew and W. Yue, "Accurate and Simple Density Functional for the Electronic Exchange Energy," *Phys. Rev. B* **33**, 8800–8802 (1986).

[49] A. D. Becke, "Density-Functional Exchange-Energy Approximation with Correct Asymptotic Behavior," *Phys. Rev. A* **38**, 3098–3100 (1988).

[50] Z. Wu and R. E. Cohen, "More Accurate Generalized Gradient Approximation for Solids," *Phys. Rev. B* **73**, 235116 (2006).

[51] J. P. Perdew and Y. Wang, "Accurate and Simple Analytic Representation of the Electron-Gas Correlation Energy," *Phys. Rev. B* **45**, 13244–13249 (1992).

[52] K. Burke, J. P. Perdew, and Y. Wang, "Derivation of a Generalized Gradient Approximation," in *Electronic Density Functional Theory: Recent Progress and New Directions*, edited by J. F. Dobson, G. Vignale, and M. P. Das (Springer, New York, 1998), pp. 81–111.

[53] J. P. Perdew, K. Burke, and M. Ernzerhof, "Generalized Gradient Approximation Made Simple," *Phys. Rev. Lett.* **80**, 891–894 (1998).

[54] S. L. Dudarev, G. A. Botton, S. Y. Savrasov, C. J. Humphreys, and A. P. Sutton, "Electron-Energy-Loss Spectra and the Structural Stability of Nickel Oxide: An LSDA+U Study," *Phys. Rev. B* **57**, 1505–1509 (1998).

[55] V. I. Anisimov, J. Zaanen, and O. K. Andersen, "Band Theory and Mott Insulators: Hubbard U Instead of Stoner I," *Phys. Rev. B* **44**, 943–954 (1991).

[56] V. I. Anisimov and O. Gunnarsson, "Density-Functional Calculation of Effective Coulomb Interactions in Metals," *Phys. Rev. B* **43**, 7570–7574 (1991).

[57] J. B. Goodenough, "Spin-Orbit-Coupling Effects in Transition-Metal Compounds," *Phys. Rev.* **171**, 466–477 (1968).

[58] M. Petersen, F. Wagner, L. Hufnagel, M. Scheffler, P. Blaha, and K. Schwarz, "Improving the Efficiency of FP-LAPW Calculations," *Comput. Phys. Commun.* **126**, 294–309 (2000).

[59] H. L. Skriver, *The LMTO Method: Muffin-Tin Orbitals and Electronic Structure* (Springer, Berlin, 2012).

[60] M. A. Ghebouli, B. Ghebouli, and M. Fatmi, "Calculation of Physical Properties of the Cubic Perovskite-Type Oxide BiScO3 Using the PP-PW Method," *Solid State Commun.* **151**, 908–915 (2011).

[61] H. Eschrig, M. Richter, and I. Opahle, "Relativistic Solid State Calculations," in *Relativistic Electronic Structure Theory - Fundamentals*, edited by P. Schwerdtfeger (Elsevier, Amsterdam, 2004), Vol. 14, pp. 723–776.

[62] N. Papanikolaou, R. Zeller, and P. H. Dederichs, "Conceptual Improvements of the KKR Method," *J. Phys.: Condens. Matter* **14**, 2799–2823 (2002).

[63] G. K. H. Madsen, P. Blaha, K. Schwarz, E. Sjöstedt, and L. Nordström, "Efficient Linearization of the Augmented Plane-Wave Method," *Phys. Rev. B* **64**, 195134 (2001).

[64] J. C. Slater, "Wave Functions in a Periodic Potential," *Phys. Rev.* **51**, 846–851 (1937).

[65] J. C. Slater, "Energy Band Calculations by the Augmented Plane Wave Method," *Adv. Quantum Chem.* **1**, 35–58 (1964).

[66] P. E. Blöchl, "Projector Augmented-Wave Method," *Phys. Rev. B* **50**, 17953–17979 (1994).

[67] O. K. Andersen, O. Jepsen, and G. Krier, "Exact Muffin-Tin Orbital Theory," in *Lectures on Methods of Electronic Structure Calculations*, edited by V. Kumar, O. K. Andersen, and A. Mookerjee (World Scientific, Singapore, 1994), pp. 63–124.

[68] D. J. Singh and L. Nordström, *Planewaves, Pseudopotentials, and the LAPW Method*, 2nd ed. (Springer, New York, 2006).

[69] B. Sahli, M. A. Ghebouli, A. Bouhemadou, and Y. Al-Douri, "Contribution à l'étude des propriétés structurales, élastiques et électroniques des pérovskites AXO3 (A= Sr, Bi, Na, K) par la méthode (FP-LAPW)," *Ann. Chim. Sci. Mat.* **39**, 1–15 (2015).

[70] F. Bowman, *Introduction to Bessel Functions* (Dover, New York, 2012).

[71] O. K. Andersen, "Linear Methods in Band Theory," *Phys. Rev. B* **12**, 3060–3083 (1975).

[72] D. D. Koelling and G. O. Arbman, "Use of Energy Derivative of the Radial Solution in an Augmented Plane Wave Method," *J. Phys. F: Met. Phys.* **5**, 2041–2054 (1975).

[73] D. R. Hamann, "Semiconductor Charge Densities with Hard-Core and Soft-Core Pseudopotentials," *Phys. Rev. Lett.* **42**, 662–665 (1979).

[74] G. Ovando, J. Morales, and J. López-Bonilla, "Three Dimensional Effective Mass Schrödinger Equation," *J. Mol. Model.* **19**, 2007–2014 (2013).

[75] D. J. Singh, "Adequacy of the Local-Spin-Density Approximation for Gd," *Phys. Rev. B* **44**, 7451–7454 (1991).

[76] S. Goedecker and K. Maschke, "Alternative Approach to Separable First-Principles Pseudopotentials," *Phys. Rev. B* **42**, 8858–8861 (1990).

[77] D. J. Singh and H. Krakauer, "H-Point Phonon in Molybdenum," *Phys. Rev. B* **43**, 1441–1444 (1991).

[78] D. J. Singh and W. E. Pickett, "Skutterudite Antimonides: Quasilinear Bands and Unusual Transport," *Phys. Rev. B* **50**, 11235–11238 (1994).

[79] T. Takeda and J. Kübler, "Linear Augmented Plane Wave Method for Self-Consistent Calculations," *J. Phys. F: Met. Phys.* **9**, 661–672 (1979).

[80] L. Smrčka, "Linearized Augmented Plane Wave Method Utilizing the Quadratic Energy Expansion of Radial Wave Functions," *Czech. J. Phys. B* **34**, 694–704 (1984).

[81] D. Shaughnessy, G. Evans, and M. Darby, "An Improved LAPW Method for the Calculation of Self-Consistent Electronic Band Structures," *J. Phys. F: Met. Phys.* **17**, 1671–1680 (1987).

[82] D. J. Singh, "Ground-State Properties of Lanthanum," *Phys. Rev. B* **43**, 6388–6392 (1991).

[83] P. Blaha, K. Schwarz, P. Sorantin, and S. B. Trickey, "Full-Potential, Linearized Augmented Plane Wave Programs for Crystalline Systems," *Comput. Phys. Commun.* **59**, 399–415 (1990).

[84] P. Blaha, K. Schwarz, G. K. H. Madsen, D. Kvasnicka, and J. Luitz, *WIEN2k: An Augmented Plane Wave + Local Orbitals Program for Calculating Crystal Properties* (Technische Universität Wien, Vienna, 2024).

[85] Koller, David; Tran, Fabien; Blaha, Peter. Improving the modified Becke-Johnson exchange potential. *Phys. Rev. B* **85**, 155109 (2012).

[86] C. Kittel, *Introduction to Solid State Physics*, 8th ed. (Wiley, Hoboken, NJ, 2005).

[87] N. W. Ashcroft and N. D. Mermin, *Solid State Physics* (Holt, Rinehart and Winston, New York, 1976).

[88] S.-H. Wei and A. Zunger, "Calculations of the Electronic and Structural Properties of ZnO," *Appl. Phys. Lett.* **85**, 166–168 (1999).

[89] Materials Project, Zinc Oxide (ZnO) - Materials Project MP-2133; https://next-gen.materialsproject.org/materials/mp-2133 .

[90] Y. Zhang, X. Y. Qin, D. Y. Li, and J. Zhang, "Effect of Rare-Earth Doping on Structural and Electronic Properties of ZnO," *J. Mater. Sci.* **48**, 863–870 (2013).

[91] A. González, J. A. Sans, F. J. Manjón, A. Segura, and C. Drasar, "Structural Distortions Induced by Rare-Earth Doping in ZnO," *Phys. Rev. B* **83**, 024418 (2011).

[92] L. Vayssieres, K. Keis, S.-E. Lindquist, and A. Hagfeldt, "Growth of ZnO Nanostructures," *J. Lumin.* **105**, 196–200 (2003).

[93] F. Birch, "Finite Elastic Strain of Cubic Crystals," *Phys. Rev.* **71**, 809–824 (1947).

[94] F. Tran and P. Blaha, "Accurate Band Gaps of Semiconductors and Insulators with a Semilocal Exchange-Correlation Potential," *Phys. Rev. Lett.* **102**, 226401 (2009).

[95] A. Y. Liu, J. K. Freericks, and W. E. Pickett, *Rare-Earth Doping of ZnO for Magnetic and Optical Applications J. Appl. Phys.* **108**, 123703 (2010).

[96] Lehlohonolo F. Koao, Francis B. Dejene, Moges Tsega, Hendrik C. Swart, *Annealed Ce3+-doped ZnO flower-like morphology synthesized by chemical bath deposition method*, *Physica B* **480**, 53–57 (2016).

[97] Soumahoro, I., Schmerber, G., Douayar, A., Colis, S., Abd-Lefdil, M., Hassanain, N., Berrada, A., Muller, D., Slaoui, A., Rinnert, H., & Dinia, A. *Structural, optical, and electrical properties of Yb-doped ZnO thin films prepared by spray pyrolysis method.*, *Journal of Applied Physics*, **109**(3), 033708 (2011).

[98] C.O.L.A.K. Hakan. *Influence of Tm2O3 doping on structural and electrical properties of ZnO*, *J. Mater. Sci. Mater. Electron.* **26**, 784–790 (2015).

[99] Ayat, Zahia. *Simulation of Electronic Properties in Metallic Hydrides.* Doctoral Thesis, Kasdi Merbah University – Ouargla, 2019.

[100] Isik, M., and Gasanly, N. M. *Gd-doped ZnO nanoparticles: Synthesis, structural and thermoluminescence properties Journal of Luminescence* **207** (2019): 220–225.

[101] A. Janotti and C. G. Van de Walle, "Fundamentals of Zinc Oxide as a Semiconductor," *Rep. Prog. Phys.* **72**, 126501 (2009).

[102] S. Lany and A. Zunger, *Anion Vacancies as a Source of Persistent Photoconductivity in II-VI and Chalcopyrite Semiconductors Phys. Rev. B* **72**, 035215 (2005).

[103] R. M. Martin, *Electronic Structure: Basic Theory and Practical Methods* (Cambridge University Press, Cambridge, 2004).

[104] F. Hübler, M. S. Brandt, M. Stutzmann, and H. C. Hofsäss, *Magnetic and Electronic Properties of Rare Earth Doped ZnO Phys. Rev. B* **76**, 245211 (2007).

[105] A. Wibowo, M. A. Marsudi, M. I. Amal, M. B. Ananda, R. Stephanie, H. Ardy, and L. J. Diguna, *ZnO nanostructured materials for emerging solar cell applications*, RSC Adv. **10**(70), 42838-42859 (2020).

[106] S. Selvaraj, M. K. Mohan, M. Navaneethan, S. Ponnusamy, and C. Muthamizhchelvan, *Synthesis and photocatalytic activity of Gd doped ZnO nanoparticles for enhanced degradation of methylene blue under visible light*, Mater. Sci. Semicond. Process. **103**, 104622 (2019).

[107] A. El Hachimi, H. Zaari, A. Benyoussef, M. El Yadari, and A. El Kenz, *First-Principles Prediction of the Magnetism of 4f Rare-Earth-Metal-Doped Wurtzite Zinc Oxide J. Rare Earths* **32**, 715–720 (2014).

[108] R. M. Sánchez Reyes, Y. Kumar, M. A. Cortés-Jácome, J. A. Toledo Antonio, X. Mathew, and N. R. Mathews, *Effect of Eu Doping on the Physical, Photoluminescence, and Photocatalytic Characteristics of ZnO Thin Films Grown by Sol-Gel Method*, Phys. Status Solidi A **214**(10), 1700229 (2017).